Targeting cellular DNA damage responses in cancer: An *in vitro*-calibrated agent-based model simulating monolayer and spheroid treatment responses to ATR-inhibiting drugs

Sara Hamis[1,2,3], James Yates[4], Mark AJ Chaplain[1], Gibin G Powathil[2,3].

[1] School of Mathematics and Statistics, University of St Andrews, St Andrews KY16 9SS, Scotland.
[2] Department of Mathematics, College of Science, Swansea University, Swansea, SA2 8PP, United Kingdom.
[3] Computational Foundry, Swansea University, Swansea, SA1 8EN, United Kingdom.
[4] Oncology R&D, AstraZeneca, Cambridge, United Kingdom.

Abstract

A systems pharmacology approach is combined with an agent-based modelling approach to simulate LoVo cells subjected to AZD6738, an ATR (ataxia telangiectasia mutated and rad3-related kinase) inhibiting anti-cancer drug that can hinder tumour proliferation by targeting cellular DNA damage responses. The agent-based model used in this study is governed by a set of empirically observable rules. By adjusting only the rules when moving between monolayer and multi-cellular tumour spheroid simulations, whilst keeping the fundamental mathematical model and parameters intact, the agent-based model is first parameterised by monolayer *in vitro* data and is thereafter used to simulate treatment responses in *in vitro* tumour spheroids subjected to dynamic drug delivery. Spheroid simulations are subsequently compared to *in vivo* data from xenografts in mice. The spheroid simulations are able to capture the dynamics of *in vivo* tumour growth and regression for approximately eight days post tumour injection.

Translating quantitative information between *in vitro* and *in vivo* research remains a scientifically and financially challenging step in preclinical drug development processes. However, well-developed *in silico* tools can be used to facilitate this *in vitro* to *in vivo* translation, and in this article we exemplify how data-driven, agent-based models can be used to bridge the gap between *in vitro* and *in vivo* research. We further highlight how agent-based models, that are currently underutilised in pharmaceutical contexts, can be used in preclinical drug development.

Keywords

DNA damage response inhibition, Agent-based model, Mathematical oncology, AZD6738.

1 Introduction

1.1 Bridging *in vitro* and *in vivo* research

Mathematical models, and corresponding *in silico* tools, can be used to simulate both *in vitro* and *in vivo* scenarios that involve cancer cell populations, or tumours, and their responses to anti-cancer treatments (Rockne et al., 2019; Bruno et al., 2020; Stephanou et al., 2018; Brady-Nicholls et al., 2020; Scott et al., 2019). However, cancer cells in an *in vitro* cell culture experience a microenvironment that is significantly different from the microenvironment experienced by cancer cells in a solid tumour *in vivo*. As these microenvironments influence cell proliferation and the delivery of oxygen, drug and nutrient molecules to cells, it follows that the dynamics of a cancer cell population *in vitro* differs from the dynamics of a solid tumour *in vivo*. Consequently, translating data obtained by *in vitro* experiments into quantitative information that can guide or predict *in vivo* experiments remains a challenging, but important, step in drug development processes. As an intermediate step between monolayer cell cultures and *in vivo* tumours, multicellular tumour spheroids (in this study referred to as spheroids) provide *in vitro* models that are able to capture certain key-features of *in vivo* tumours such as intratumoural heterogeneity resulting from nutrient-gradients and resource-limited tumour growth (Nunes et al., 2019).

Agent-based models (ABMs) are used in many applications in mathematical biology but are underutilised in the context of pharmaceutical drug development (Cosgrove et al., 2015). An ABM consists of multiple, distinct agents that may interact with each other and their microenvironment. There exists different types of ABMs. For example, agents can be deformable or of fix size, and agent movements and neighbourhood-interactions can be constrained by an underlying lattice geometry (on-lattice models) or not (off-lattice models). Combining ABMs with hybrid modelling techniques allows for the integration of discrete and continuous variables describing tumour dynamics on multiple scales. A thorough review on various types of hybrid ABMs used to simulate tumour growth is provided by Rejniak and Anderson (Rejniak and Anderson, 2011). Furthermore, a number of open-source *in silico* tools, such as Chaste (Mirams et al., 2013), CompuCell3D (Swat et al., 2012) and PhysiCell (Ghaffarizadeh et al., 2018), are freely available to facilitate the implementation of ABMs.

In this study, we introduce a novel modelling approach that uses an agent-based mathematical model, specifically a cellular automaton (CA), to bridge the gap between *in vitro* monolayer and spheroid research as a step towards bridging the gap between *in vitro* and *in vivo* research, as is conceptually illustrated in Figure 1. For a broader scope discussion on how to develop, calibrate and validate mathematical models that can predict novel anti-cancer therapies, we refer the reader to a recent article by Brady and Enderling (Brady and Enderling, 2019). In the ABM at the core of this modelling approach, an agent consists of one cancer cell or a group of cancer cells, where the behaviour and fate of each agent is governed by a set of empirically observable and well-established *modelling rules* that incorporate both intracellular and microenvironmental dynamic variables, as is described throughout Section 2. To account for differences between monolayer and spheroid scenarios, the modelling rules are adjusted when moving between monolayer and spheroid simulations. By only adjusting the rules, whilst keeping the fundamental mathematical model and parameters intact, when moving between monolayer and spheroid simulations, the mathematical framework can first be parameterised by monolayer data and thereafter be

used to simulate spheroid treatment responses. To exemplify this modelling approach, we here simulate LoVo (human colon carcinoma) cells subjected to the anti-cancer drug AZD6738. The ABM is first calibrated by monolayer *in vitro* data and is thereafter used to simulate *in vitro* spheroids subjected to dynamic drug delivery. Spheroid simulations are subsequently compared to xenograft *in vivo* data. The *in vitro* and *in vivo* data used in this study are gathered from previous work by Checkley *et al.* (Checkley et al., 2015). The ABM used in this study is an extension of a CA introduced by Powathil *et al.* (Powathil et al., 2012b).

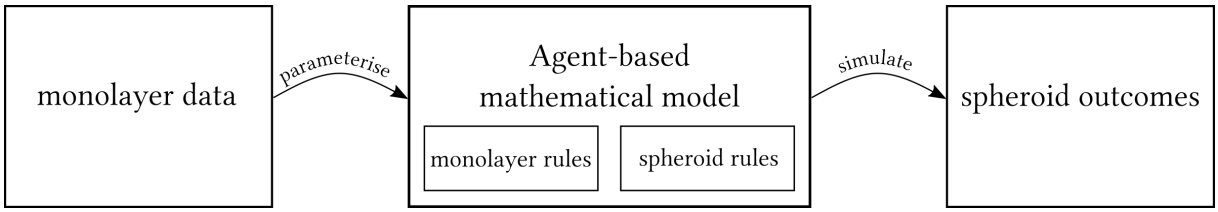

Figure 1: A schematic of the mathematical modelling approach used in this study. An agent-based mathematical model, that distinguishes between *in vitro* monolayer and spheroid modelling rules, is formulated. The mathematical model is first parameterised by *in vitro* monolayer data and is thereafter used to simulate spheroid scenarios.

1.2 DNA damage response inhibiting drugs

The deoxyribonucleic acid (DNA) in human cells is perpetually exposed to, potentially harmful, influences that can be derived from both exogenous and endogenous sources and events (Minchom et al., 2018; Sundar et al., 2017). Exogenous sources include ultraviolet radiation, ionising radiation and chemotherapeutic drugs, whilst erroneous DNA replication is an example an endogenous event yielding DNA damage (Minchom et al., 2018). Regardless of the source, a multitude of intracellular events are triggered when the DNA in a cell becomes damaged. Cells may, for example, respond to DNA damage by activating DNA repair mechanisms, cell cycle arrest or, in cases of severe DNA damage, apoptosis (Carrassa and Damia, 2017). Such cellular responses to DNA damage are mainly governed by the DNA damage response (DDR), which comprises a complex network of signalling pathways (Carrassa and Damia, 2017). The DDR has many functionalities and, amongst other things, it monitors DNA integrity and repairs DNA damage in order to maintain genomic stability in cells. The DDR also governs DNA replication, cell cycle progression, and apoptosis (Minchom et al., 2018; Nam et al., 2018). When DNA repair in a cell is needed, the DDR activates relevant effector proteins (Minchom et al., 2018). Included in the group of DDR-associated effector proteins are approximately 450 proteins (Nam et al., 2018), out of which the two main regulators for cell cycle checkpoints are ataxia telangiectasia mutated kinase (ATM) and ataxia telangiectasia mutated and rad3-related kinase (ATR) (Sundar et al., 2017). ATM and ATR belong to the enzyme family phosphatidyilinositol-3-OH-kinases (PI3K), and they both play central roles when cells respond to DNA damage (Carrassa and Damia, 2017). In this work, we study the effects of an anti-cancer drug, namely AZD6738, that works by inhibiting ATR activity.

DNA lesions in form of single-strand breaks are a common result of replication stress, and the

repair of single-strand DNA breaks is mainly attributed to ATR activity. A drug that inhibits ATR activity consequently inhibits the repair of single-strand DNA breaks post replication stress. Cancer cells are associated with high replication stress and consequently ATR inhibitors have, during the last decade, been explored as anti-cancer agents (Minchom et al., 2018; Carrassa and Damia, 2017; Mei et al., 2019). With the premise that inhibiting DNA damage responses should increase the effect of some other main therapy, DDR inhibitors have been explored as both radiotherapy and chemotherapy treatment intensifiers (Carrassa and Damia, 2017; Mei et al., 2019). Two well-studied ATR inhibitors are AZD6738 and VX-970. AZD6738 is an oral ATR inhibitor, and its anti-tumour potential has been demonstrated in preclinical *vitro* and *in vivo* xenograft studies for various ATM deficient cell lines, including ATM deficient lung cancer, chronic lymphocytic leukemia and metastatic adenocarcinoma of the colon (Checkley et al., 2015; Sundar et al., 2017; Foote et al., 2018). Combination treatments that combine AZD6738 with either radiotherapy or chemotherapy have produced synergistic results in preclinical settings (Sundar et al., 2017), and AZD6738 is currently being evaluated in clinical phase I/II trials (Minchom et al., 2018; Mei et al., 2019). VX-970 is an intravenous ATR inhibitor (Tu et al., 2018) that has demonstrated tumour controlling effects in a phase I clinical trial, both as a monotherapy and in combination with the chemotherapy drug carboplatin (Minchom et al., 2018). A summarising table of clinical trials involving ATR-inhibitors can be found in an article by Mei *et al.* (Mei et al., 2019).

2 Model and Method

An ABM, specifically a CA, is used to model an *in vitro* monolayer population of cancer cells, or a multi-cellular tumour spheroid that evolves in time and space. The model describes the behaviour of cancer cells using a set of modelling rules. In order to account for differences between monolayer and spheroid scenarios, these rules are adjusted when moving between monolayer and spheroid simulations, as is described throughout Section 2. Taking a minimal parameter approach, we aim to use as few rules and parameters as possible to capture the nature of the regarded system. We here chose to include model rules and parameters that pertain to the cells' doubling time and cell cycle (see Section 2.2), cell proliferation on the lattice (see Section 2.3), the distribution of oxygen and drugs across the lattice (see Sections 2.4 and 2.5 respectively) and cellular responses to local oxygen and drug concentrations (see Sections 2.4 and 2.6 respectively). In this work, details concerning nutrient distribution and its effect on tumour growth are not included. Instead, under a simplifying modelling assumption, the diffusion of oxygen forms a surrogate for the distribution of nutrients. Differences between monolayer and spheroid simulation modelling rules are pictorially summarised in Section 2.8, and monolayer-calibrated model parameters are listed in Table 1.

The *in vitro* and *in vivo* data used in this study are gathered from previous work by Checkley *et al.* (Checkley et al., 2015). In the regarded *in vitro* experiments, populations of LoVo cells were plated and subjected to AZD6738, where population sizes of up to roughly 4000 cells were reported (Checkley et al., 2015). In the *in vivo* experiments, LoVo cells were subcutaneously injected in flanks of female Swiss nude mice in order to produce human tumour xenografts, and AZD6738 treatments started when the tumours had reached a volume of 0.2-0.3 cm^3 (Checkley

et al., 2015). Here, we regard treatment responses in terms two dynamic variables: population or tumour size and percentage of DNA-damaged (i.e. γH2AX-positive) cells. The *in vitro* and *in vivo* data used in our current study are available in the Supplementary Material (Supplementary Material, S1).

2.1 Cellular automaton lattice

In the model, one *agent* corresponds to one cancer cell (in the monolayer simulation) or, due to computational costs, one group of cancer cells (in the spheroid simulation). The behaviour and fate of each agent is governed by a set of rules that incorporate both intracellular and environmental dynamic variables using multiscale modelling techniques (Rejniak and Anderson, 2011). At the start of an *in silico* experiment, one initial agent is placed in the centre of the lattice. This initial agent produces daughter agents and ultimately gives rise to a heterogeneous population of agents. When the population has reached an appropriate size (chosen to match the *in vitro* and *in vivo* data in the monolayer and spheroid simulations respectively), AZD6738 anticancer treatments commence. The CA lattice is a square lattice, and every lattice point is either empty or occupied by one agent. If a lattice point is empty, it consists of extracellular solution providing nutrients to cells . In the monolayer simulations, the dispersion of any molecules across the lattice is modelled as instantaneous, and thus the extracellular solution is considered to render the entire lattice homogeneous in terms drug and oxygen concentrations at all times. In the spheroid simulations, however, drug and oxygen molecules are modelled as gradually diffusing over the spheroid and its local environment, and consequently the spheroid lattice will be heterogeneous in terms of drug and oxygen concentrations. Oxygen and drug distribution across the lattice are further discussed in Sections 2.4 and 2.5 respectively. Since Checkley *et al.* (Checkley et al., 2015) provide monolayer cell population sizes in units of number of cells, and *in vivo* tumour sizes in cm^3, we here choose to measure simulated monolayer and spheroid sizes using cell counts and volumes respectively. The cellular automata lattices are chosen accordingly, as is described below.

Monolayer lattice: Cell populations evolve on a two-dimensional square lattice with 100×100 lattice points, where the spacing in both spatial directions, x_1 and x_2, corresponds to one cell diameter.

Spheroid lattice: We simulate (only) a central cross section of the spheroid as an, approximately circular, disk of cells living on a two-dimensional square lattice. This lattice is specifically an $\tilde{L} \times \tilde{L} = 1000 \times 1000$ square lattice, with a spacing in both spatial directions $\tilde{x}_1$ and $\tilde{x}_2$ equal to 40μm. The dimensions are chosen in order to allow our agent-based model to simulate the required physical dimensions, whilst keeping computational costs low. Post simulation time, the two-dimensional cross section of cells is extrapolated to represent a three-dimensional spheroid. This disk-to-spheroid extrapolation process is outlined in the Supplementary Material (Supplementary Material, S4).

2.2 Cell cycle model

In order to capture the influence of ATR and the ATR inhibitor AZD6738 on the cell cycle, we use a probabilistic, rule-based cell cycle model adapted from previous mathematical (non-agent-based) work by Checkley *et al.* (Checkley et al., 2015). As illustrated in Figure 2, this cell cycle model can be represented as a graph with nodes (cell cycle phases or states) that are connected via various paths (phase/state transitions). A cell can be in an undamaged state (G1, S or G2/M), a replication stress-induced DNA damaged state (D-S) or a dead state, where the cause of cell death is unrepaired replication stress. As ATR is active in the checkpoint in the intra-S phase of the cell cycle, both under undamaged circumstances and in response to DNA damage (Carrassa and Damia, 2017), ATR inhibition will inhibit the cell from progressing to the G2/M state in the mathematical cell cycle model. A cell can take different possible paths through the cell cycle graph, and every time that paths fork, random number generation (from a uniform distribution) determines which path will be taken. Every cell commences its life in the G1 state, but thereafter a cell can enter either the S state or the damaged S (D-S) state. The probability that a cell enters the D-S state is denoted Π_{D-S} and is calibrated by *in vitro* data (Checkley et al., 2015). If a cell enters the D-S state, it has a chance to repair itself and enter the S state. If there is no drug in the system, this repair is always achieved, however the repair path is inhibited by the presence of the drug AZD6738. The higher the drug-concentration, the more unlikely it is that a cell in the D-S state will successfully repair itself to the S state. If a cell in the D-S state fails to repair, it is sentenced to die. Whether a cell in state D-S repairs or dies is decided by comparing a random number, generated from a uniform distribution, to the cell's survival probability, which is influenced by the local drug concentration $C(\bar{x}, t)$, as is described in detail in Section 2.6. A cell that has successfully reached the S state continues to the G2/M state, after which it duplicates and starts over in the G1 state again, ready to perform another cell cycle.

In order to allow for asynchronous populations, each agent i on the lattice is assigned an individual doubling time τ_i, where τ_i is a random number generated from a normal distribution with mean value μ and standard deviation σ. Each agent is attributed an individual cell cycle clock, that determines when the agent should progress to a subsequent state in the cell cycle model. Progression to a subsequent state occurs once an agent has spent a certain fraction of its doubling time in its current state. The fraction of the doubling time spent in the G1, S (including D-S) and G2/M states are respectively denoted Θ_{G1}, Θ_S and $\Theta_{G2/M}$, where these values are approximate and chosen from literature to match values for typical human cells with a rapid doubling time of 24 hours so that $\Theta_{G1} = 11/24$, $\Theta_S = 8/24$ and $\Theta_{G2/M} = 5/24$ (Cooper and Hausman, 2007). The fraction of an agent's doubling-time spent in the D-S state, Θ_{D-S}, is on the other hand fitted by *in vitro* data produced by Checkley *et al.* (Checkley et al., 2015), as outlined in the Supplementary Material (Supplementary Material, S2). Monolayer and spheroid cell cycle modelling rules are described below.

Monolayer cell cycle model rules: One agent corresponds to one cancer cell that is assigned an individual doubling time τ_i. The cell cycle path taken by cell i is governed by random number generations specific to that cell.

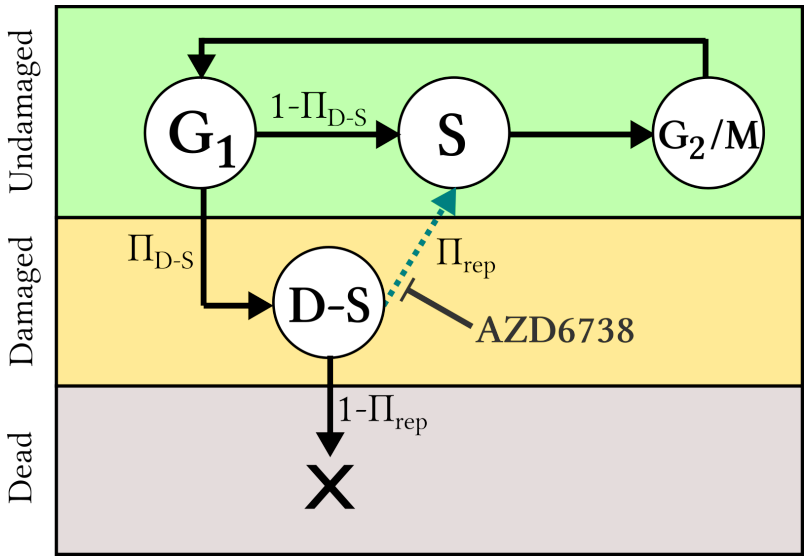

Figure 2: Cell cycle model: An agent, i.e a cell (in the monolayer simulation) or a group of cells (in the spheroid simulation), progresses through various states of the cell cycle, where the states correspond to cell cycle phases and are shown as nodes in the graph. Viable (undamaged or damaged) states are shown in circles, whilst the dead state is shown as a cross. Paths illustrate transitions between states, and symbols next to the paths denote the probabilities that the corresponding paths will be taken. The dashed path can be inhibited by an ATR inhibiting drug, such as AZD6738.

Spheroid cell cycle model rules: One agent comprises a group of identical cancer cells. Each agent is assigned an individual doubling time, τ_i, and thus all cells belonging to agent i progress simultaneously and uniformly through the cell cycle model. Random number generations specific to agent i determine which path the agent takes through the cell cycle.

2.3 Cell proliferation

When an agent has completed the mitosis state in the cell cycle model, a secondary agent, namely a daughter agent, is produced. Each daughter agent is placed on a random lattice point in the (approximately circular) neighbourhood of its parental agent. To accomplish circular-like growth, the model stochastically alternates between placing daughter agents on Moore and von Neumann neighbourhoods of parental agents, as is pictorially described in the Supplementary Material (Supplementary Material, S3). A daughter agent is allowed to be placed on, up to, a νth order neighbourhood of its parental agent, but lower order neighbourhoods (i.e. neighbourhoods closer to the parent) are prioritised and populated first. Modelling rules concerning monolayer and spheroid cell proliferation are outlined below.

Monolayer proliferation rules: In the experimental *in vitro* setup, there is no spatial constraint or nutrient deficiency that is inhibiting cell division within the time-course of the experiment. Consequently cells are allowed to divide freely in the monolayer model and we set ν to be equal to infinity (with the restriction that agents can not be placed outside the lattice in the *in silico* implementation). Although this non-local placement of daughter cells neglects physics, we are not considering spatial heterogeneity in the monolayer simulation and therefore cell location does not affect the evaluated simulation results.

Spheroid proliferation rules: *In vivo* tumours and *in vitro* spheroids typically consist of a core with non-proliferating cells and a shell of proliferating cells. To accommodate for this, a daughter agent (representing a group of daughter cells) is allowed to be placed on up to a third order (approximately circular) neighbourhood of its parental agent, so that $\tilde{\nu} = 3$, in accordance with previous mathematical models (Powathil et al., 2012b). For the spheroid simulation regarded in our current study, $\tilde{\nu} = 3$ matches the experimental *in vivo* data. However, for other experiments, the value of $\tilde{\nu}$ may be adjusted to fit the specific cell-line and modelling scenario at hand. When an agent is in the G1 phase of the cell cycle, it scans its environment to see if it has enough resources, in terms of space and nutrients, to commence the process of producing a daughter cell. If not, the cell enters the quiescent phase (Alarcon et al., 2004). Thus in the model, when an agent is in the G1 phase, it continues to progress through the cell cycle model, provided that some free space is available on the lattice within its $\tilde{\nu}$th neighbourhood. If this is not the case, the agent exits the cell cycle to enter a quiescent state G0. Should neighbourhood space be made available again, here as a result of anticancer targeting, quiescent agents may re-enter the cell cycle.

2.4 Oxygen distribution and influence on cells

Tumour growth and treatment responses are highly influenced by intratumoural oxygen levels (Hu et al., 2010; Liapis et al., 2015; Peeters et al., 2015) and severely hypoxic (cancer) cells proliferate slower than do well-oxygenated cells (Alarcon et al., 2004).

Monolayer oxygen distribution and responses: In the mathematical monolayer model, all cells are assumed to be well-oxygenated in accordance with the experimental *in vitro* setup performed by Checkley *et al.* (Checkley et al., 2015). Consequently, neither oxygen dynamics nor cellular responses to oxygen levels are incorporated in the monolayer model.

Spheroid oxygen distribution and responses: Within solid tumours, oxygen concentrations typically vary and hypoxic regions are common tumour features (Peeters et al., 2015; Hamis et al., 2020a; Sun et al., 2012). Oxygen gradients are also observed in *in vitro* tumour spheroids (Voissiere et al., 2017), thus oxygen dynamics across the CA lattice are here described using a mechanistic diffusion equation, where the oxygen concentration in location $\bar{x}$ at time t is denoted by $K(\bar{x}, t)$ where

$$\frac{\partial K(\bar{x}, t)}{\partial t} = \nabla \cdot (D_K(\bar{x}, t)\nabla K(\bar{x}, t)) + r_K m(\bar{x}, t) - \phi_K K(\bar{x}, t) cell(\bar{x}, t). \tag{1}$$

The first term in Equation 1 describes oxygen diffusion across the CA lattice, the second term is an oxygen supply term and the third term describes oxygen uptake by cells. Accordingly, $D_K(\bar{x}, t)$ is the oxygen diffusion coefficient, and r_K and ϕ_K are supply and consumption coefficients respectively. The diffusion coefficient for oxygen is known from literature to be 2.5×10^{-5} cm^2s^{-1} (Powathil et al., 2012b). Assuming that oxygen diffuses slower inside the spheroid than outside the spheroid, the oxygen diffusion coefficient is divided by a factor 1.5 if there is a cell in location $\bar{x}$ at time t (Powathil et al., 2012b). The binary factor $m(\bar{x}, t)$ is 1 if the regarded location $\bar{x}$ is outside the spheroid boundary at time t and 0 otherwise, i.e. $m(\bar{x}, t)$ is 1 if the regarded lattice point is not occupied by an agent nor completely surrounded by agents, thus oxygen is here modelled as supplied from 'outside the boundary of the spheroid'. Similarly, the binary factor $cell(\bar{x}, t)$ is 1 if there is a viable (non-dead) cell in location $\bar{x}$ at time t, and 0 otherwise (Powathil et al., 2012b). Equation 1 is coupled with no-flux boundary conditions, thus the total amount of oxygen in the system will fluctuate over time (Powathil et al., 2012a). A scaled oxygen variable $\hat{K}(\bar{x}, t)$ is introduced in order to express oxygenation levels in percentages (%) between 0% and 100%. This scaled oxygen value is computed at every unique time step t_u by

$$\hat{K}(\bar{x}, t_u) = \frac{K(\bar{x}, t_u)}{max_{\bar{x}, t_u} K(\bar{x}, t_u)} \cdot h, \tag{2}$$

where $max_{\bar{x}, t_u} K(\bar{x}, t_u)$ denotes the maximum occurring $K(\bar{x}, t_u)$-value at the time point t_u and h is a scaling factor that is included in order to classify cells with oxygen levels of 10%, or less, as hypoxic (Powathil et al., 2012b; Hamis et al., 2020a). Low cellular oxygen levels have been shown to delay cell cycle progression by inducing arrest in, particularly, the G1 phase of the cell cycle (Alarcon et al., 2004). Consequently, in our model, hypoxic cells display arrest (i.e. delay) in the G1 phase of the cell cycle. In mechanistic Tyson-Novak type cell cycle models

(Tyson and Novak, 2001; Novak and Tyson, 2003, 2004), the cell cycle is governed by a system of ordinary differential equations (ODEs) in which the G1 phase can be inherently elongated under hypoxic conditions by incorporating hypoxia-induced factors into the ODEs (Powathil et al., 2012b). In the mathematical model discussed in this paper, however, we use agent-attributed clocks to model cell cycle progression and thus, in order to achieve a longer G1-phase under hypoxic conditions, we introduce a G1 delay factor (G1DF) (Hamis et al., 2020a) where

$$G1DF(\hat{K}(x,t)) = \begin{cases} 2 & \text{if } 0\% \leq \hat{K}(x,t) < 1\%, \\ a_1 + \frac{a_2}{a_3 + \hat{K}(\bar{x},t)} & \text{if } 1\% \leq \hat{K}(x,t) \leq 10.5\%, \\ 1 & \text{otherwise.} \end{cases} \tag{3}$$

The G1DF is an approximation for how much the G1 phase is expanded in time as a function of cellular oxygen concentration. It is matched to fit data points extracted from a previous mathematical study by Alarcon *et al.* (Alarcon et al., 2004), in which a Tyson-Novak cell cycle model is extended to incorporate the action of p27, a protein that is up-regulated under hypoxia and delays cell cycle progression. Data-fitting yields the parameter values $a_1 = 0.9209, a_2 = 0.8200, a_3 = -0.2389$ (Hamis et al., 2020a). Thus the fraction of an agent's doubling time spent in the G1 state is $G1DF(\hat{K}(\bar{x},t)) \cdot \Theta_{G1}$, where $G1DF(\hat{K}(\bar{x},t)) = 1$ for normoxic cells.

2.5 Drug distribution across the lattice

Drug distribution significantly varies between monolayer and spheroid settings. In the regarded monolayer setup, the drug concentration can be regarded as homogeneous, whilst heterogeneous drug concentrations must be accounted for when simulating drug distribution across the spheroid. Drug uptake and receptor dynamics is omitted in the model, the drug response of an agent is instead influenced by the drug concentration in the lattice point that it occupies.

Monolayer drug distribution: In the *in vitro* experiments performed by Checkley *et al.* (Checkley et al., 2015), plated cell populations of roughly 1000 cells were treated with AZD6738 in the solvent dimethylsulfoxide (DMSO). In the mathematical model, we approximate the drug distribution across the CA lattice to be instantaneous (occurring at treatment time T_0) and homogeneous. We furthermore assume that the drug has a half-life time that exceeds the time course of the experiment, and note that there is no other drug elimination from the *in vitro* system. In our mathematical model, this is equivalent to there being no drug decay or elimination, hence the drug concentration $C(\bar{x},t)$, in location $\bar{x}$ at time t is simply given by

$$C(\bar{x},t) = \begin{cases} 0 \text{ everywhere} & \text{if } t < T_0, \\ \mathbb{C} \text{ everywhere} & \text{if } t \geq T_0, \end{cases} \tag{4}$$

where $\mathbb{C}$ denotes the applied drug concentration (in units of molarity).

Spheroid drug distribution: The spheroid scenarios simulated in this study are compared to the in vivo experiments performed by Checkley et al. (Checkley et al., 2015), in which the drug AZD6738, or vehicle in the control case, were administered via oral gavage once per day

to female Swiss nude mice. Therefore we include dynamic drug delivery and drug decay in our spheroid simulations. In the mathematical spheroid model, we consider the drug to diffuse through the spheroid from its surrounding, creating a drug gradient within the spheroid. This drug dynamics is modelled using a partial differential equation (PDE), where the concentration of AZD6738 at location $\bar{x}$ at time t is denoted by $C(\bar{x}, t)$ such that

$$\frac{\partial C(\bar{x}, t)}{\partial t} = \nabla \cdot \big(D_{AZD}(\bar{x}, t)\nabla C(\bar{x}, t)\big) + p(\bar{x}, t) - \eta_{AZD} C(\bar{x}, t), \tag{5}$$

where D_{AZD} is the diffusion coefficient of the drug AZD6738, and the supply coefficient $p(\bar{x}, t)$ is greater than zero at drug administration times only for lattice points outside the tumour. Assuming first order kinetics for drug elimination, the drug decay constant η_{AZD} is matched to the reported half-life time of 6 hours for AZD6738 *in vivo* (Vendetti et al., 2015; Dale and Rang, 2007). Note that the drug decay term here represents all drug elimination from the system, both metabolic and that caused by excretion.

The diffusion rate of a drug is predominantly affected by the molecular size of the drug. More specifically, the diffusion coefficient of a drug is inversely proportional to the square root of the molecular weight of the drug, so that large molecules diffuse more slowly than do small molecules (Dale and Rang, 2007). Using this assumption, the drug diffusion coefficient D_{AZD} is set in relation to the oxygen diffusion coefficient D_{0_2}, as is done in previous mathematical studies (Powathil et al., 2012b). Thus the relationship between the diffusion coefficients corresponds to the square of the inverse relationship between the molecular weights, such that

$$\frac{D_{AZD}}{D_{0_2}} = \frac{\sqrt{\text{molecular weight}(\mathrm{O}_2)}}{\sqrt{\text{molecular weight}(\text{AZD})}} = \sqrt{\frac{31.998\text{g/mol}}{412.512\text{g/mol}}} \approx 0.27851, \tag{6}$$

where the molecular weights are collected from the PubChem database (Kim et al., 2019). Details regarding pharmacokinetics are outside the scope of this study, bioavailability is instead calibrated using extreme case drug scenarios, as described in the Supplementary Material (Supplementary Material, S2).

2.6 Drug responses

AZD6738 inhibits DNA repair from the D-S state to the S state in the cell cycle model, as illustrated in Figure 2, and, in our model, maximal drug effect corresponds to complete repair inhibition. The drug effect is modelled using an agent-based adaptation of the sigmoid Emax model (Holford, 2017), a note on the choice of drug model is included in the Supplementary Material (Supplementary Material, S6). In the ABM-adapted sigmoidal Emax model used here, the drug effect on a cell in position $\bar{x}$ at time t is given by

$$E(\bar{x}, t) = E_{max} \frac{C(\bar{x}, t)^{\gamma}}{EC_{50}^{\gamma} + C(\bar{x}, t)^{\gamma}}, \tag{7}$$

where the drug concentration in lattice point $\bar{x}$ at time t is given by $C(\bar{x}, t)$. E_{max} denotes the maximal drug effect, here corresponding to complete repair inhibition ($E_{max} = 1$), EC_{50} denotes

the drug concentration required to achieve half of the maximal drug effect ($0.5 \cdot E_{max}$) and γ is the Hill-exponent (Holford, 2017). EC_{50} and γ are fitted from the *in vitro* data, as outlined in the Supplementary Material (Supplementary Material, S2). When an agent is scheduled to progress from the D-S state in the cell cycle, it has a probability $\Pi_{rep} \in [0,1]$ to repair, where Π_{rep} is determined by the local drug concentration so that

$$\Pi_{rep}(\bar{x}, t) = 1 - E(\bar{x}, t). \tag{8}$$

Note that in the absence of drugs, the repair probability is 1. When a cell dies, it is transformed into a membrane-enclosed 'cell-corpse' (Dale and Rang, 2007). In an *in vivo* setting, this cellular debris is digested by macrophages but in an *in vitro* setting such 'cell-corpses' may linger on the lattice during the course of the experiment. Post the lethal event (i.e. the D-S to S repair failure) a cell is declared 'dead' in the model after a time $T_{L \to D}$ has passed (where L stands for 'lethal event' and D stands for 'death'). The parameter $T_{L \to D}$ is calibrated by *in vitro* experiments. The differences between modelling rules for monolayer and spheroid drug responses are described below.

Monolayer drug responses: After failure to repair from the D-S state, a cell (i.e. and agent) is considered to be dead after a time $T_{L \to D}$ has passed. However, a dead cell is never physically removed from the lattice.

Spheroid drug responses: In order to emulate *in vivo*-like removal of dead cancer cells, an agent (i.e. a group of cells) is declared to be dead and is removed from the lattice after an amount of time $T_{L \to D}$ post the lethal event (failure to repair).

2.7 Parameters

The parameters used in the mathematical model are calibrated by monolayer *in vitro* data, this calibration process is described in the Supplementary Material (Supplementary Material, S2). In the context of quantitative pharmacology, knowledge about a model's robustness is crucial (Visser et al., 2014), therefore we have provided results from the uncertainty and sensitivity analysis in the Supplementary Material (Supplementary Material, S9). We performed three different uncertainty and sensitivity analyses techniques, suitable for agent-based models with stochastic elements, namely (*i*) consistency analysis, (*ii*) robustness analysis and (*iii*) Latin hypercube analysis (Hamis et al., 2020b; Alden et al., 2013). Detailed descriptions on how to perform and interpret these techniques are available in an introductory uncertainty and sensitivity analyses review (Hamis et al., 2020b). In accordance with the performed consistency analysis, we run 100 simulations per *in silico* experiment in order to formulate results (in terms of mean values and standard deviations) that mitigate uncertainty originating from intrinsic model stochasticity.

2.8 Differences between monolayer and spheroid modelling rules

Modelling rules are adjusted when moving between monolayer and spheroid simulations. Differences between monolayer and spheroid rules are pictorially summarised in Figure 3. A note

Section	Parameter	Calibrated Value
2.2	μ, σ	24 h, 0.5 h
	Π_{D-S}, θ_{D-S}	0.75, 0.03
2.6	EC_{50}, γ	1 μM, 2
	$T_{L\rightarrow D}$	τ_i

Table 1: *In vitro* calibrated parameters.

on the simplifying modelling assumptions that we have used in this study is provided in the Supplementary Material (Supplementary Material, S5).

2.9 Implementation

The mathematical model is implemented in an in-house C++ (Stroustrup, 1995) framework, in which PDEs are solved using explicit finite difference methods. Simulation cell-maps are visualised using ParaView (Ayachit and Utkarsh, 2015) and data analysis, as well as uncertainty and sensitivity analyses, are performed in MATLAB (MATLAB, 2019).

3 Results

The mathematical framework is first calibrated by *in vitro* monolayer data. Thereafter, spheroids subjected to dynamic drug delivery and the removal of dead cells are simulated. Spheroid simulations are then compared to *in vivo* treatment responses in human tumour xenografts. Two model outputs are considered in the *in silico* simulations: the fraction of DNA damaged cells in the system and the size of the cancer cell population or tumour spheroid over time. Note that, in the model, a cell is classified as DNA-damaged if it is in the D-S state of the cell cycle depicted in Figure 2. In the experimental setup, DNA damaged cells are labeled as γ-H2AX positive (Checkley et al., 2015).

3.1 Simulating monolayer experiments

The mathematical framework is parameterised by monolayer *in vitro* data produced by Checkley *et al.* (Checkley et al., 2015). In the *in vitro* experiments, populations of LoVo (human colon carcinoma) cells were exposed to the ATR inhibiting drug AZD6738. The results in Figure 4 show the evolution of the monolayer cell population over time in terms of percentage of DNA damaged, *i.e.* γH2AX-positive, cells (Left) and in terms of cell count (Right). AZD6738 drugs are given at 0 hours, when the cell population has reached a size of approximately 1000 cells. Simulated response curves for six different drug concentrations, including the zero-drug concentration control case, are shown. Also shown in Figure 4 are simulation standard deviations, *in vitro* data (Checkley et al., 2015) and results from a mathematical compartment-ODE model presented by Checkley *et al.* (Checkley et al., 2015) describing the same experimental scenario.

Using a minimal-parameter modelling approach, the mathematical framework is calibrated to fit *in vitro* data points without introducing any variable model parameters. This calibration process is described in the Supplementary Material (Supplementary Material, S2). Our results demonstrate that, post *in vitro* monolayer parameterisation, our mathematical framework is

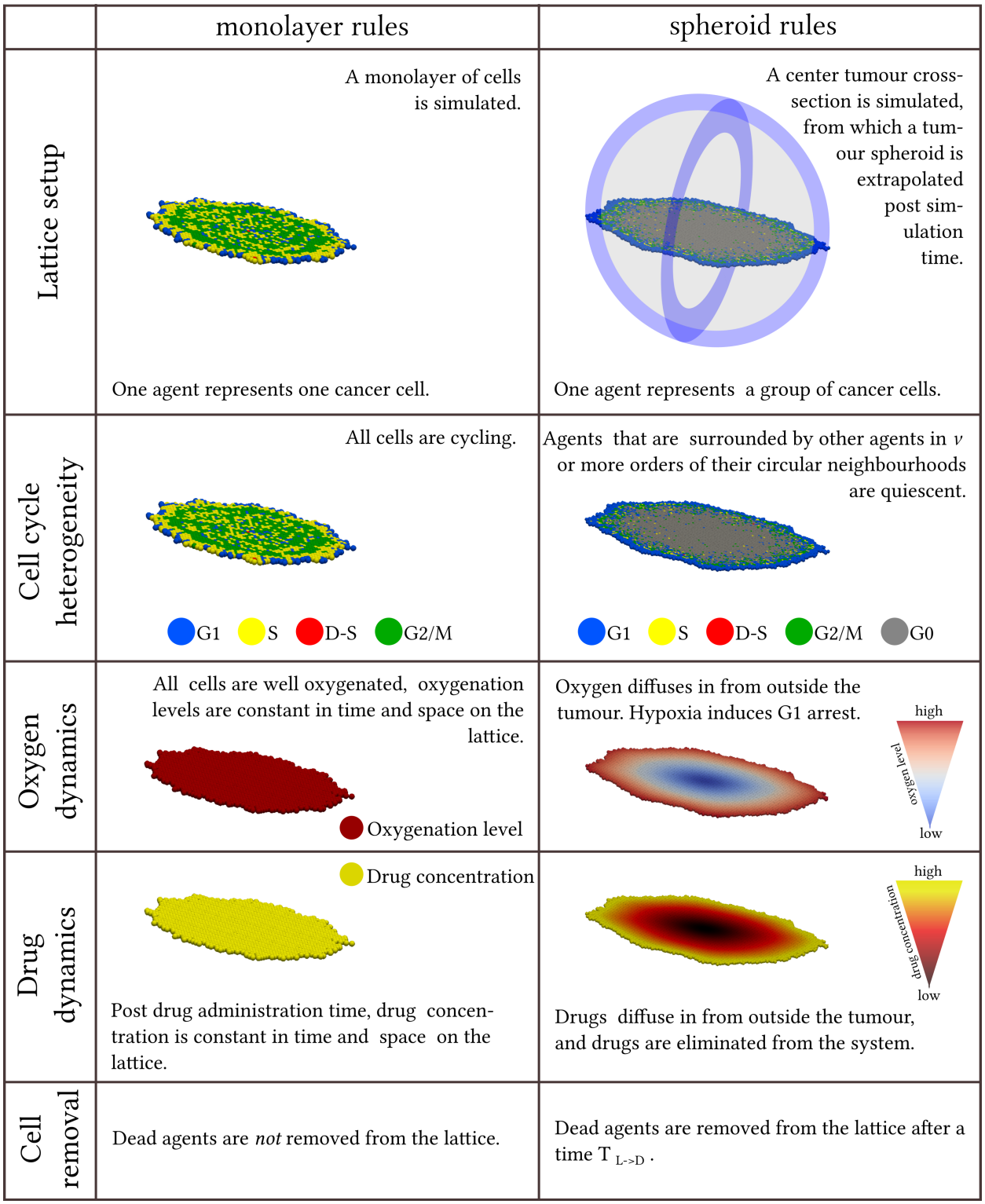

Figure 3: A summary of the differences between the monolayer and spheroid modelling rules used in the mathematical framework.

able to capture the qualitative nature of *in vitro* monolayer LoVo cell population growth and drug (AZD6738) responses. Figure 4 (Left) demonstrates that the model is able to qualitatively reproduce the asymptotic fraction of DNA damaged cells in the system but fails to match early *in vitro* data points. The sensitivity analysis demonstrates that the treatment timing (in relation to the overall cell cycle phase composition of the cancer cell population) notably influences treatment responses in terms of percentage of γH2AX-positive cells. This indicates that in the *in vitro* experiments, a large fraction of the cells would have been in the DNA damaged D-S state when, or shortly after, the drug was applied. The data from Checkley *et al.* (Checkley et al., 2015) indicates cell cycle synchronisation amongst cells, explaining the step-wise curves in Figure 4. The experimental error bars in Figure 4 (Right) and the numerical cell count data, available in Table S1 in the Supplementary Material (Supplementary Material, S1), demonstrate that the doubling time of the cell population drastically decreased towards the end of the *in vitro* experiment and, consequently, our agent-based model was not able to replicate cell count data at 72 hours as the modelling rules and parameters were not updated over time. Residual plots, comparing ABM simulation results to *in vitro* data and Checkley *et al.*'s (Checkley et al., 2015) compartment-ODE model are available in the Supplementary Material (Supplementary Material, S7). In an effort to quantify how the models match the data, the Root Mean Square Error (RMSE) is here computed between N simulation mean values and data mean values so that RMSE$=\left(\sum_{i=1}^{N}(sim_i - data_i)^2/N\right)^{1/2}$. When comparing DNA damage simulation results to data, the ABM model yields an RMSE of 11.6 units of percent, whilst the compartment-ODE model yields an RMSE of 14.6 units of percent. When comparing cell count simulation results to data, however, the ABM RMSE is 644 cells whilst the compartment-ODE RMSE is 495 cells.

3.2 Simulating spheroid experiments

Post *in vitro* monolayer calibration, the mathematical framework is used to simulate spheroid experiments, that are compared to the *in vivo* experiments performed by Checkley *et al.* (Checkley et al., 2015) in which LoVo xenografts, that are injected in mice flanks, are treated with AZD6738 once daily for 14 days. The results in Figure 5 show AZD6738 drug responses in terms of the percentage of DNA damaged (γH2AX-positive) cells (Figure 5 Left) and spheroid/tumour volume (Figure 5 Right). Simulated response curves to three different drug doses (0, 25 and 50 mg/kg) and *in vivo* data are provided in Figure 5.

Figure 5 (Right) demonstrates that our simulated spheroid results qualitatively agrees with the *in vivo* results reported by Checkley et al. (Checkley et al., 2015) for approximately 12 days post tumour injection for control case tumours, and for approximately 8 days post tumour injection for tumours subjected to drugs. This can be explained by the fact that the behaviour of the agents in our current model does not change over time, when in fact tumours are highly adaptable and responsive to external pressures. It follows that details pertaining to tumour growth and drug sensitivity may vary over time, and in future work the agent-based model used in this study can be updated to incorporate variable modelling rules and parameters. Residual plots, comparing ABM simulation results to *in vivo* data (Checkley et al., 2015) are available in the Supplementary Material (Supplementary Material, S7) for DNA damage and spheroid/tumour volume evaluations. The RMSE for DNA results is 3.57 units of percent. For the spheroid/tumour volume simulation results, the RMSE is 0.038 cm^3 up to and including 8

days, but 0.16 cm^3 for the full 14 day simulations.

4 Discussion

Simulation results obtained in this study were compared to *in vitro* and *in vivo* data and , furthermore, to previous mathematical modelling results produced by Checkley *et al.* (Checkley et al., 2015). In their study, Checkley *et al.* (Checkley et al., 2015) modelled tumour responses to AZD6738 using coupled ordinary differential equations, where a pharmacokinetic/pharmacodynamic (PK/PD) model of tumour growth was integrated with a mechanistic cell cycle model. Their model is predictive of *in vivo* xenograft studies and is being used to quantitatively predict dose and scheduling responses in a clinical Phase I trial design (Checkley et al., 2015). Our modelling results qualitatively agree with those produced by Checkley *et al.* (Checkley et al., 2015), although two different modelling approaches have been taken: Checkley *et al.* (Checkley et al., 2015) regard the tumour as one entity with different compartments whilst we here use a bottom-up modelling approach and regard the tumour as consisting of multiple, distinct agents.

Moving drug-response investigations from *in vitro* to *in vivo* settings is a key step involved in the process of moving a drug from *bench-to-bedside*. However, *in vivo* data are often sparse, as gathering *in vivo* data is associated with practical, financial and ethical constraints. Plentiful and adaptable *in silico* data are, on the other hand, easy to produce, and can thus be used as epistemic complements to sparse *in vivo* data. Well-formulated *in silico* tools can be extended to investigate various dose-schedule scenarios in order to guide *in vitro* and *in vivo* experiments. Such *in silico* experiments may provide a testbed for simulating various mono and combination therapies. In this study we aimed to capture treatment responses in tumour spheroids (with dynamic drug delivery and the removal of dead cells) using monolayer data and modelling rules that are based on chosen "fundamental" principles that describe how cancer cells in a system behave. Although our spheroid simulations were able to qualitatively mimic the dynamics of *in vivo* xenografts at early time-points (up to 8 days) post tumour injection, the model did not match data at later time points. This is to expected, as the effects of certain biological processes that are present *in vivo*, but not *in vitro* (*e.g.,* angiogenesis), do not impact the tumour volume instantly after tumour injection. Thus the spheroid model can, in future work, be extended to more accurately simulate *in vivo* scenarios. For example, stromal tumours cells, angiogenesis and metastasis can be included in the model. Moreover, further heterogeneity amongst cancer cells can be incorporated, pertaining to *e.g.* drug resistance-related variables. In order to account for mechanical aspects of tumour growth, the approximated cancer cell population/tumour growth model, which allows for daughter agents being placed on non-adjacent lattice point of the parental agent, can be updated to a more realistic proliferation model. Pharmacokinetic details, drug uptake and receptor dynamics can be included in order to make the drug model more detailed. In order to realistically simulate *in vivo* tumours, effects of the host's immune system can furthermore be incorporated in the model.

The ABM considered in this study is an extension of a mathematical model that has previously been used to study tumour growth and treatment responses to chemotherapy, radiotherapy, hyperthermia and hypoxia-activated prodrugs (Powathil et al., 2012b; Hamis et al., 2020a; Powathil et al., 2015; Hamis et al., 2018, 2019; Bruningk et al., 2018). In recent years, several

ABMs have been developed for the purpose of describing various aspects of cancer dynamics (Metzcar et al., 2019), and it should be noted that the modelling approach proposed in Figure 1 is not conceptually limited to usage with the ABM described in this study. The choice of ABM should be influenced by the research question at hand, the desired level of model details and the available data. Examples of data-driven ABMs are available in a recent review article by Chamseddine and Rejniak (Chamseddine and Rejniak, 2020) discussing hybrid models, and hybrid modelling techniques, used in the field of mathematical oncology today.

Data-driven modeling, exploitation of existing data and proof-of-concept studies are important steps involved in current and future procedure for enabling mathematical modeling in systems medicine, as argued in a report by Wolkenhauer *et al.* (Wolkenhauer et al., 2014). A pipeline for predicting therapy outcomes using data-driven mathematical modelling is proposed by Brady and Enderling (Brady and Enderling, 2019) in a recent publication. Despite the fact that mathematical modelling is becoming increasingly popular in the pharmaceutical industry, there are not that many ABMs present in the pharmaceutical scene (Cosgrove et al., 2015). We argue that this is a missed opportunity in the context of oncology, as ABMs naturally capture the heterogeneous nature of tumours, which is known to complicate treatments. As multiscale ABMs organically enable the integration of data across various scales in time and space, it follows that they are useful to the interdisciplinary team that wishes to combine data and knowledge from its team members. Following interdisciplinary collaborations between clinicians, biologists and mathematicians, mathematical modelling may be used to enable *in silico* informed drug development.

Declarations

Funding

SH was supported by the Medical Research Council [grant code MR/R017506/1] and Swansea University PhD Research Studentship.

Conflicts of interest

The authors declare that they have no conflict of interest.

Availability of data and material (data transparency)

All *in vitro/in vivo* data used in this study is available in the Supplementary Material (Supplementary Material, S1). All *in vitro/in vivo* data used in this study is gathered from previous work by Checkley *et al.* (Checkley et al., 2015).

Code availability (software application or custom code)

– *This paragraph will be updated upon the manuscript progressing through the peer-review process.*

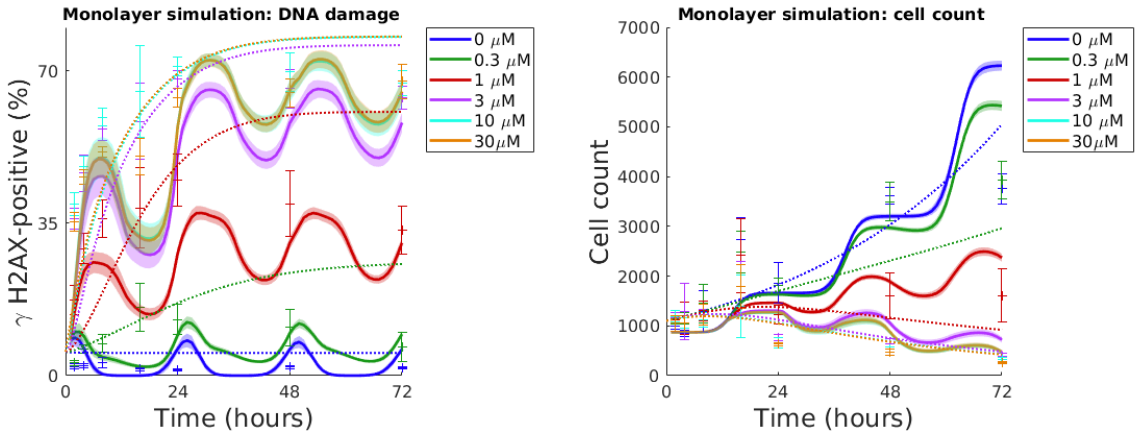

Figure 4: Simulated monolayer drug response curves are compared to *in vitro* data and mathematical results from a previously published compartment-ODE model by Checkley *et al.* (Checkley et al., 2015). LoVo cells are exposed to drug (AZD6738) at 0 hours. Left: The percentage of γH2AX-positive (DNA-damaged) cells in the system over time. Right: Cell count over time. Simulated mean values and standard deviations for 100 *in silico* runs are shown with solid lines and shaded ribbons respectively. *In vitro* data in form of mean values and standard deviations are demonstrated with center points and error bars (Checkley et al., 2015). Compartment-ODE model results are represented by dotted lines.

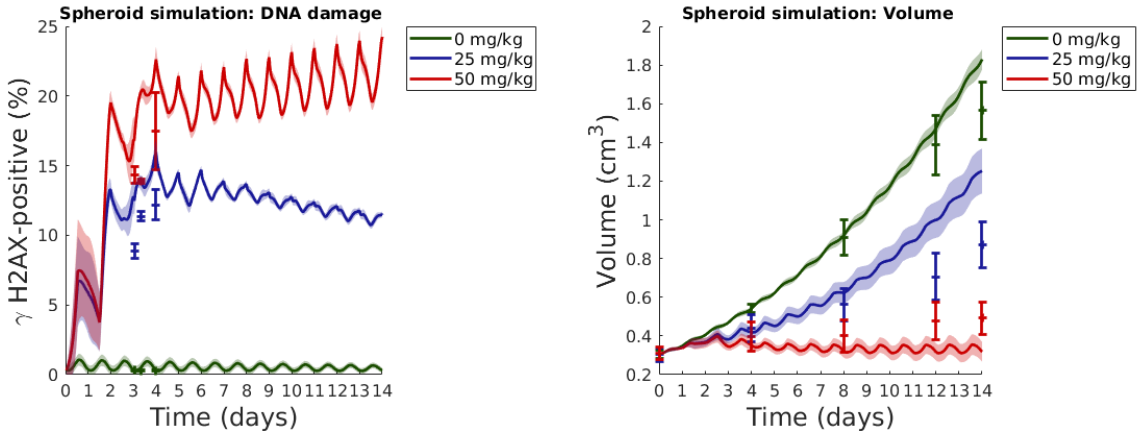

Figure 5: Simulated spheroid drug response curves are compared to *in vivo* xenograft data. The simulations mimic the *in vivo* experiment in which LoVo xenografts are exposed to drug (AZD6738) once daily for 14 days. Left: The percentage of γH2AX-positive (DNA-damaged) cells in the spheroid/xenograft over time. Right: Spheroid/xenograft volume over time. Simulated (spheroid) mean values and standard deviations for 100 *in silico* runs are shown with solid lines and shaded ribbons respectively. *In vivo* data in form of mean values and standard errors are demonstrated with center points and error bars (Checkley et al., 2015).

References

Alarcon, T., Byrne, H.M., Maini, P.K., 2004. A mathematical model of the effects of hypoxia on the cell-cycle of normal and cancer cells. *J. Theor. Biol.* **229**(3), 395–411.

Alden, K., Read, M., Timmis, J., Andrews, P.S., Veiga-Fernandes, H., Coles, M., 2013. Spartan: a comprehensive tool for understanding uncertainty in simulations of biological systems. *PLoS Comput. Biol.* **9**(2), e1002916.

Ayachit, Utkarsh, 2015. The ParaView Guide: A Parallel Visualization Application, ISBN: 978-1930934306. *Kitware* .

Brady, R., Enderling, H., 2019. Mathematical Models of Cancer: When to Predict Novel Therapies, and When Not to. *Bull. Math. Biol.* **81**(10), 3722–3731.

Brady-Nicholls, R., Nagy, J.D., Gerke, T.A., Zhang, T., Wang, A.Z., Zhang, J., Gatenby, R.A., Enderling, H., 2020. Prostate-specific antigen dynamics predict individual responses to intermittent androgen deprivation. *Nat Commun* **11**(1), 1750.

Bruningk, S., Powathil, G., Ziegenhein, P., Ijaz, J., Rivens, I., Nill, S., Chaplain, M., Oelfke, U., Ter Haar, G., 2018. Combining radiation with hyperthermia: a multiscale model informed byin vitroexperiments. *J R Soc Interface* **15**(138).

Bruno, R., Bottino, D., de Alwis, D.P., Fojo, A.T., Guedj, J., Liu, C., Swanson, K.R., Zheng, J., Zheng, Y., Jin, J.Y., 2020. Progress and Opportunities to Advance Clinical Cancer Therapeutics Using Tumor Dynamic Models. *Clin. Cancer Res.* **26**(8), 1787–1795.

Carrassa, L., Damia, G., 2017. DNA damage response inhibitors: Mechanisms and potential applications in cancer therapy. *Cancer Treat. Rev.* **60**, 139–151.

Chamseddine, I.M., Rejniak, K.A., 2020. Hybrid modeling frameworks of tumor development and treatment. *Wiley Interdiscip Rev Syst Biol Med* **12**(1), e1461.

Checkley, S., MacCallum, L., Yates, J., Jasper, P., Luo, H., Tolsma, J., Bendtsen, C., 2015. Bridging the gap between in vitro and in vivo: Dose and schedule predictions for the ATR inhibitor AZD6738. *Sci Rep* **5**, 13545.

Cooper, G., Hausman, R., 2007. The Cell-A Molecular Approach 4th edition .

Cosgrove, J., Butler, J., Alden, K., Read, M., Kumar, V., Cucurull-Sanchez, L., Timmis, J., Coles, M., 2015. Agent-Based Modeling in Systems Pharmacology. *CPT Pharmacometrics Syst Pharmacol* **4**(11), 615–629.

Dale, M.M., Rang, H.P., 2007. Rang & Dale's pharmacology . *Edinburgh: Churchill Livingstone* .

Foote, K.M., Nissink, J.W.M., McGuire, T., Turner, P., Guichard, S., Yates, J.W.T., Lau, A., Blades, K., Heathcote, D., Odedra, R., Wilkinson, G., Wilson, Z., Wood, C.M., Jewsbury, P.J., 2018. Discovery and Characterization of AZD6738, a Potent Inhibitor of Ataxia Telangiectasia

Mutated and Rad3 Related (ATR) Kinase with Application as an Anticancer Agent. *J. Med. Chem.* **61**(22), 9889–9907.

Ghaffarizadeh, A., Heiland, R., Friedman, S.H., Mumenthaler, S.M., Macklin, P., 2018. PhysiCell: An open source physics-based cell simulator for 3-D multicellular systems. *PLoS Comput. Biol.* **14**(2), e1005991.

Hamis, S., Kohandel, M., Dubois, L.J., Yaromina, A., Lambin, P., Powathil, G.G., 2020a. Combining hypoxia-activated prodrugs and radiotherapy in silico: Impact of treatment scheduling and the intra-tumoural oxygen landscape. *PLoS Comput. Biol.* **16**(8), e1008041.

Hamis, S., Nithiarasu, P., Powathil, G.G., 2018. What does not kill a tumour may make it stronger: In silico insights into chemotherapeutic drug resistance. *J. Theor. Biol.* **454**, 253–267.

Hamis, S., Powathil, G.G., Chaplain, M.A.J., 2019. Blackboard to Bedside: A Mathematical Modeling Bottom-Up Approach Toward Personalized Cancer Treatments. *JCO Clin Cancer Inform* **3**, 1–11.

Hamis, S., Stratiev, S., Powathil, G.G., 2020b. Uncertainty and sensitivity analyses methods for agent-based mathematical models: An introductory review. *The Physics of Cancer: Research Advances, ed. Bernard Gerstman, Singapore: World Scientific Publishing. Preprint: arXiv:1911.08429* .

Holford, N., 2017. Pharmacodynamic principles and the time course of immediate drug effects. *Transl Clin Pharmacol* **4**, 157–161.

Hu, J., Handisides, D.R., Van Valckenborgh, E., De Raeve, H., Menu, E., Vande Broek, I., Liu, Q., Sun, J.D., Van Camp, B., Hart, C.P., Vanderkerken, K., 2010. Targeting the multiple myeloma hypoxic niche with TH-302, a hypoxia-activated prodrug. *Blood* **116**(9), 1524–1527.

Kim, S., Chen, J., Cheng, T., Gindulyte, A., He, J., He, S., Li, Q., Shoemaker, B.A., Thiessen, P.A., Yu, B., Zaslavsky, L., Zhang, J., Bolton, E.E., 2019. PubChem 2019 update: improved access to chemical data. *Nucleic Acids Res.* **47**(D1), D1102–D1109.

Liapis, V., Labrinidis, A., Zinonos, I., Hay, S., Ponomarev, V., Panagopoulos, V., DeNichilo, M., Ingman, W., Atkins, G.J., Findlay, D.M., Zannettino, A.C., Evdokiou, A., 2015. Hypoxia-activated pro-drug TH-302 exhibits potent tumor suppressive activity and cooperates with chemotherapy against osteosarcoma. *Cancer Lett.* **357**(1), 160–169.

MATLAB, 2019. version 1.8.0_202 (R2019n). The MathWorks Inc., Natick, Massachusetts.

Mei, L., Zhang, J., He, K., Zhang, J., 2019. Ataxia telangiectasia and Rad3-related inhibitors and cancer therapy: where we stand. *J Hematol Oncol* **12**(1), 43.

Metzcar, J., Wang, Y., Heiland, R., Macklin, P., 2019. A Review of Cell-Based Computational Modeling in Cancer Biology. *JCO Clin Cancer Inform* **3**, 1–13.

Minchom, A., Aversa, C., Lopez, J., 2018. Dancing with the DNA damage response: next-generation anti-cancer therapeutic strategies. *Ther Adv Med Oncol* **10**, 1758835918786658.

Mirams, G.R., Arthurs, C.J., Bernabeu, M.O., Bordas, R., Cooper, J., Corrias, A., Davit, Y., Dunn, S.J., Fletcher, A.G., Harvey, D.G., Marsh, M.E., Osborne, J.M., Pathmanathan, P., Pitt-Francis, J., Southern, J., Zemzemi, N., Gavaghan, D.J., 2013. Chaste: an open source C++ library for computational physiology and biology. *PLoS Comput. Biol.* **9**(3), e1002970.

Nam, A.R., Jin, M.H., Park, J.E., Bang, J.H., Oh, D.Y., Bang, Y.J., 2018. Therapeutic Targeting of the DNA Damage Response Using an ATR Inhibitor in Biliary Tract Cancer. *Cancer Res Treat* .

Novak, B., Tyson, J.J., 2003. Modelling the controls of the eukaryotic cell cycle. *Biochem. Soc. Trans.* **31**(Pt 6), 1526–1529.

Novak, B., Tyson, J.J., 2004. A model for restriction point control of the mammalian cell cycle. *J. Theor. Biol.* **230**(4), 563–579.

Nunes, A.S., Barros, A.S., Costa, E.C., Moreira, A.F., Correia, I.J., 2019. 3D tumor spheroids as in vitro models to mimic in vivo human solid tumors resistance to therapeutic drugs. *Biotechnol. Bioeng.* **116**(1), 206–226.

Peeters, S.G., Zegers, C.M., Biemans, R., Lieuwes, N.G., van Stiphout, R.G., Yaromina, A., Sun, J.D., Hart, C.P., Windhorst, A.D., van Elmpt, W., Dubois, L.J., Lambin, P., 2015. TH-302 in Combination with Radiotherapy Enhances the Therapeutic Outcome and Is Associated with Pretreatment [18F]HX4 Hypoxia PET Imaging. *Clin. Cancer Res.* **21**(13), 2984–2992.

Powathil, G., Kohandel, M., Milosevic, M., Sivaloganathan, S., 2012a. Modeling the spatial distribution of chronic tumor hypoxia: implications for experimental and clinical studies. *Comput Math Methods Med* **2012**, 410602.

Powathil, G.G., Gordon, K.E., Hill, L.A., Chaplain, M.A., 2012b. Modelling the effects of cell-cycle heterogeneity on the response of a solid tumour to chemotherapy: biological insights from a hybrid multiscale cellular automaton model. *J. Theor. Biol.* **308**, 1–19.

Powathil, G.G., Swat, M., Chaplain, M.A., 2015. Systems oncology: towards patient-specific treatment regimes informed by multiscale mathematical modelling. *Semin. Cancer Biol.* **30**, 13–20.

Rejniak, K.A., Anderson, A.R., 2011. Hybrid models of tumor growth. *Wiley Interdiscip Rev Syst Biol Med* **3**(1), 115–125.

Rockne, R.C., Hawkins-Daarud, A., Swanson, K.R., Sluka, J.P., Glazier, J.A., Macklin, P., Hormuth, D.A., Jarrett, A.M., Lima, E.A.B.F., Tinsley Oden, J., Biros, G., Yankeelov, T.E., Curtius, K., Al Bakir, I., Wodarz, D., Komarova, N., Aparicio, L., Bordyuh, M., Rabadan, R., Finley, S.D., Enderling, H., Caudell, J., Moros, E.G., Anderson, A.R.A., Gatenby, R.A., Kaznatcheev, A., Jeavons, P., Krishnan, N., Pelesko, J., Wadhwa, R.R., Yoon, N., Nichol, D., Marusyk, A., Hinczewski, M., Scott, J.G., 2019. The 2019 mathematical oncology roadmap. *Phys Biol* **16**(4), 041005.

Scott, J.G., Maini, P.K., Anderson, A.R.A., Fletcher, A.G., 2019. Inferring Tumour Proliferative Organisation from Phylogenetic Tree Measures in a Computational Model. *Syst. Biol.* .

Stephanou, A., Fanchon, E., Innominato, P.F., Ballesta, A., 2018. Systems Biology, Systems Medicine, Systems Pharmacology: The What and The Why. *Acta Biotheor.* **66**(4), 345–365.

Stroustrup, B., 1995. The C++ Programming Language. *Addison-Wesley* .

Sun, J.D., Liu, Q., Wang, J., Ahluwalia, D., Ferraro, D., Wang, Y., Duan, J.X., Ammons, W.S., Curd, J.G., Matteucci, M.D., Hart, C.P., 2012. Selective tumor hypoxia targeting by hypoxia-activated prodrug TH-302 inhibits tumor growth in preclinical models of cancer. *Clin. Cancer Res.* **18**(3), 758–770.

Sundar, R., Brown, J., Ingles Russo, A., Yap, T.A., 2017. Targeting ATR in cancer medicine. *Curr Probl Cancer* **41**(4), 302–315.

Swat, M.H., Thomas, G.L., Belmonte, J.M., Shirinifard, A., Hmeljak, D., Glazier, J.A., 2012. Multi-scale modeling of tissues using CompuCell3D. *Methods Cell Biol.* **110**, 325–366.

Tu, X., Kahila, M.M., Zhou, Q., Yu, J., Kalari, K.R., Wang, L., Harmsen, W.S., Yuan, J., Boughey, J.C., Goetz, M.P., Sarkaria, J.N., Lou, Z., Mutter, R.W., 2018. ATR Inhibition Is a Promising Radiosensitizing Strategy for Triple-Negative Breast Cancer. *Mol. Cancer Ther.* **17**(11), 2462–2472.

Tyson, J.J., Novak, B., 2001. Regulation of the eukaryotic cell cycle: molecular antagonism, hysteresis, and irreversible transitions. *J. Theor. Biol.* **210**(2), 249–263.

Vendetti, F.P., Lau, A., Schamus, S., Conrads, T.P., O'Connor, M.J., Bakkenist, C.J., 2015. The orally active and bioavailable ATR kinase inhibitor AZD6738 potentiates the anti-tumor effects of cisplatin to resolve ATM-deficient non-small cell lung cancer in vivo. *Oncotarget* **6**(42), 44289–44305.

Visser, S.A., de Alwis, D.P., Kerbusch, T., Stone, J.A., Allerheiligen, S.R., 2014. Implementation of quantitative and systems pharmacology in large pharma. *CPT Pharmacometrics Syst Pharmacol* **3**, e142.

Voissiere, A., Jouberton, E., Maubert, E., Degoul, F., Peyrode, C., Chezal, J.M., Miot-Noirault, E., 2017. Development and characterization of a human three-dimensional chondrosarcoma culture for in vitro drug testing. *PLoS ONE* **12**(7), e0181340.

Wolkenhauer, O., Auffray, C., Brass, O., Clairambault, J., Deutsch, A., Drasdo, D., Gervasio, F., Preziosi, L., Maini, P., Marciniak-Czochra, A., Kossow, C., Kuepfer, L., Rateitschak, K., Ramis-Conde, I., Ribba, B., Schuppert, A., Smallwood, R., Stamatakos, G., Winter, F., Byrne, H., 2014. Enabling multiscale modeling in systems medicine. *Genome Med* **6**(3), 21.

Targeting cellular DNA damage responses in cancer: An *in vitro*-calibrated agent-based model simulating monolayer and spheroid treatment responses to ATR-inhibiting drugs

Sara Hamis[1,2,3], James Yates[4], Mark AJ Chaplain[1], Gibin G Powathil.[2,3]

[1] School of Mathematics and Statistics, University of St Andrews, St Andrews KY16 9SS, Scotland.
[2] Department of Mathematics, College of Science, Swansea University, Swansea, SA2 8PP, United Kingdom.
[3] Computational Foundry, Swansea University, Swansea, SA1 8EN, United Kingdom.
[4] Oncology R&D, AstraZeneca, Cambridge, United Kingdom.

– Supplementary Material

S1. Experimental data

S2. Model parameterisation

S3. Proliferation of agents on the lattice

S4. Cross-section to tumour spheroid extrapolation

S5. A note on simplifying modelling assumptions

S6. A note on the choice of drug model

S7. Residual plots

S8. Spheroid waterfall plot

S9. Uncertainty and sensitivity analyses

S1 Experimental data

The experimental *in vitro* and *in vivo* data used in our current study are gratefully gathered from a previous study performed by Checkley *et al.* (Checkley et al., 2015). *In vitro* data are listed in Table S1 and *in vivo* data are listed in Tables S2 and S3.

Time (hours)	Cell count	Std.Dev (count)	γH2AX-positive (%)	Std. Dev (%)
0μM (control)				
2	996	59.72	2.14	0.56
4	850	62.30	2.20	0.45
8	1287.5	417.59	2.90	1.22
16	2742.75	439.69	1.44	0.33
24	1857.5	409.39	1.29	0.32
48	3605.25	167.38	1.93	0.44
72	3753	311.17	1.71	0.21
0.3 μM				
2	1081.88	53.63	2.93	0.59
4	1040.75	217.96	6.15	1.00
8	1447.25	392.45	7.41	1.99
16	2479.5	414.02	15.68	5.56
24	1805.63	161.41	12.91	3.42
48	3497.63	385.19	11.08	4.18
72	3928.25	376.08	6.57	3.30
1 μM				
2	1129.63	58.26	17.35	3.31
4	1153.63	331.31	29.12	3.47
8	1303.88	199.72	36.05	4.35
16	2420.25	744.38	38.51	9.25
24	1226.38	185.58	45.01	6.01
48	1600.38	456.80	39.47	7.47
72	1612.88	540.55	33.47	5.46
3 μM				
2	1171.14	97.71	36.01	2.42
4	1291.38	567.63	46.47	4.09
8	1224.63	113.30	56.72	2.62
16	1784.38	513.06	58.41	8.81
24	765.75	70.76	68.07	2.05
48	638.75	112.54	65.90	4.40
72	392.63	67.64	63.82	2.67
10 μM				
2	1191.13	110.15	39.38	2.62
4	1056.63	106.72	47.98	2.32
8	1113.63	144.42	59.35	1.99
16	1396	633.86	65.21	10.48
24	654.5	100.26	71.02	2.10
48	525.29	43.93	69.75	4.42
72	326.63	47.73	67.25	2.87
30 μM				
2	1055.13	155.16	35.37	2.21
4	1049.13	147.96	45.66	1.75
8	1228.75	211.96	51.37	1.11
16	1794.88	435.42	50.35	4.19
24	629	27.12	63.92	2.15
48	469.63	61.26	64.92	3.25
72	265.13	22.26	67.63	3.96

Table S1: *In vitro* data gathered from a previous study by Checkley *et al.* (Checkley et al., 2015).

Time (hours)	γH2AX-positive (%)	Std. Error (%)
0 mg/kg (control)		
74	0.3200	0.0320
80	0.2770	0.0300
96	0.2970	0.0340
25 mg/kg QD		
74	8.8579	0.5364
80	11.3692	0.3272
96	12.1945	1.0949
50 mg/kg QD		
74	14.3417	0.6278
80	13.8967	0.1401
96	17.4986	2.7558

Table S2: *In vivo* data for DNA damage gathered and adapted from a previous study published by Checkley *et al.* (Checkley et al., 2015).

Time (hours)	Volume (cm^3)	Std. Error (cm^3)
0 mg/kg (control)		
168	0.3028	0.0219
264	0.5189	0.0465
360	0.9095	0.0934
456	1.3857	0.1554
504	1.5646	0.1483
25 mg/kg QD		
168	0.3037	0.0342
264	0.4411	0.0704
360	0.5617	0.0840
456	0.7064	0.1221
504	0.8701	0.1187
50 mg/kg QD		
168	0.3106	0.0332
264	0.3971	0.0768
360	0.4002	0.0817
456	0.4783	0.0966
504	0.4923	0.0846

Table S3: *In vivo* data for tumour volume gathered and adapted from a previous study published by Checkley *et al.* (Checkley et al., 2015).

S2 Model parameterisation

Using a minimal-parameter approach, seven model parameters are calibrated using the *in vitro* data previously produced by Checkley *et al.* (Checkley et al., 2015), as listed in Table 1 in Section 2.7 in the main paper. Parameter sensitivity is explored in the sensitivity analysis (Section 5 of the supplementary material). The calibration process is outlined in Sections S2.1 through to S2.4. The spheroid calibration is described in Section S2.5.

S2.1 Cell doubling

In the model, the doubling time of a cell i is denoted τ_i, where τ_i is stochastically picked from a normal distribution with mean value μ and standard deviation σ. Thus μ corresponds to the

average cell doubling time and σ corresponds to how synchronised the cells are. If σ is zero, then all cells have perfectly synchronised cell cycles and duplicate at the same time. Higher σ values achieve less synchronised cell cycles amongst cells and smoother cell count growth curves over time. The control case (i.e. no drug) cell count data is used to estimate μ and σ.

By observing the control case cell count data in Table S1, we note that the cell population roughly doubles between 2 and 24 hours (indicating an average cell doubling time, or μ, of approximately 22 hours, which is less than 24 hours). Furthermore, the cell population also roughly doubles between 24 and 48 hours (indicating that μ is approximately 24 hours). However, in the last 24-hour interval, between 48 and 72 hours, the control population increases by less than 5% (indicating that μ is more than 24 hours). From these three observations, we choose to make the modelling assumption that the average doubling time for cells should be around 24 hours, and σ-values in the parameter range [22,26] hours are investigated *in silico*. Due to the synchronised nature of the cell count data, σ-values between 0 and 2.5 hours were investigated *in silico*, where $\sigma = 0$ h corresponds to completely synchronised cells and $\sigma = 2.5$ h achieves a smooth cell count growth curve. After an iterative process of tuning parameters and running *in silico* experiments, the calibrated values are set to be $\mu = 24$ hours and $\sigma = 0.5$ hours. As discussed in the main article, the ABM can be improved to better fit wet lab data by including variable parameter values or rules, that are updated over time. However, in the current stage of our work, we decided to fix μ and σ.

S2.2 Cell cycle progression

The *in vitro* data provides information on how many cells are in the damaged S state via the biomarker γH2AX. For the control case, the number of γH2AX positive cells in our mathematical model depends on two variables: (1) the probability (Π_{D-S}) that a cell enters the D-S state and (2) the amount of time ($\Theta_{D-S} \cdot \tau_i$) spent in the D-S state prior to repairing. Recall that Θ_{D-S} is the fraction of a cell's doubling time (τ_i) spent in the D-S state. As a first step, *in silico* experiments are performed in which we find various parameter pairs (Π_{D-S}, Θ_{D-S}) that agree with the control data. We thereafter note that the *in vitro* drug effect saturates for concentrations 3, 10 and 30 μM and assume that the maximal dose (30 μM) yields 100% D-S to S repair inhibition. Thus a second step we test the variable pairs (Π_{D-S}, Θ_{D-S}) for this 'maximal drug and no repair' scenario *in silico*, and we match these *in silico* results to the 30 μM *in vitro* data. Here, we only use data from early time points (time $<$ 12 hours) in order to avoid the influence that dying cells have on the data and model outputs. After iterative *in silico* testing, the variable pair (Π_{D-S}, Θ_{D-S}) that best fits these both extreme cases is $\Pi_{D-S} = 0.75$ and $\Theta_{D-S} = 0.03$. The first extreme case refers to the 'no drug' *in silico* experiment matched to the *in vitro* control data, where we assume that all D-S cells repair to state S. The second extreme case refers to the 'maximum drug' *in silico* experiment matched to the 30μM control data, where we assume that no D-S cells repair to state S.

S2.3 Drug response

Drug effects are modelled using the sigmoid E-max model (Holford, 2017), where the drug effect E is a function of the drug concentration C, so that

$$E(C) = E_{max} \cdot \frac{C^{\gamma}}{EC_{50}^{\gamma} + C^{\gamma}},$$

where E_{max} denotes the maximal drug effect. Here we set $E_{max} = 1$ to corresponds to total D-S to S repair inhibition. EC_{50} denotes the drug concentration that achieves half of the maximal drug effect and γ is the Hill-coefficient. If drug effect is plotted over time, the EC_{50}-value determines the asymptotic behaviour of the effect whilst the γ-value determines how quickly the asymptotic value is reached.

From the *in vitro* data, we note that the drug concentration 1 μM achieves roughly half of the total drug effect in terms of γH2AX-positive cells. (Note from Table S1 that when the drug concentration is 10 μM or 30 μM, the percentage of γH2AX-positive cells is roughly 67% at 72 hours, and when the drug concentration is 1 μM, the percentage of γH2AX-positive cells is roughly 33% at 72 hours. Furthermore the lower drug concentration of 0.3 μM yields a percentage of roughly 7% γH2AX-positive at 72 hours, and the higher drug concentration of 3 μM yields a percentage of roughly 64% γH2AX-positive at 72 hours. Consequently, we use 0.3 μM as a lower bound and 3 μM as an upper bound for the parameter range in which we seek EC_{50}, and EC_{50} values in the range [0.3 μM, 3 μM] are investigated with various Hill coefficients to fit *in vitro* data for all (non-control) drug concentrations. In order to avoid the impact that dying cells have on the data used parameterise EC_{50} and γ, only early *in vitro* data (time $<$ 12 hours) is used to guide the calibration. After iterative *in silico* testing, the best variable pair (EC_{50}, γ) is determined to be $EC_{50} = 1$ μM and $\gamma = 2$.

S2.4 Cell death

In the *in vitro* experiments, cells that are damaged (but not yet dead) are γH2AX-positive. In the model, the time it takes between the 'lethal event' (i.e. a cell's failure to repair) and a cell being 'dead' is denoted $T_{L\to D}$ and is matched from the *in vitro* experiment. After noting the asymptotic behaviour of the *in vitro* data, both in terms of cell damage and cell count, we estimate that the rate of cell elimination should roughly correspond to the rate of cell production, and thus $T_{L\to D}$ should be in the same order of magnitude as the doubling time. Consequently, values of $T_{L\to D}$ between 0 and 2 τ_i are explored *in silico* after which $T_{L\to D} = \tau_i$ is chosen as it best matches the *in vitro* data for all tested (non-control) drug concentrations.

S2.5 Spheroid calibration

For the control case, the spheroid model is directly calibrated by the *in vitro* data, and no further calibration is needed. For drug concentrations larger than 0 μM, we use the *in vivo* data for the highest administered drug dose to calibrate the model in order to disregard details concerning pharmacokinetics and bioavailability. In future work, our model can be integrated with pharmacokinetic modelling techniques.

S3 Proliferation of Agents on the Lattice

When an agent divides, it places a daughter agent on the lattice. To achieve an approximately circular population growth on the square lattice, the placement of daughter agents alternates between following the von Neumann (Figure S1(a)) and Moore (Figure S1(a)) convention. The lattice points that are directly adjacent to the lattice point occupied by the parental agent (i.e. the agent that is dividing and thus producing a daughter cell) constitute the 1st order (von Neumann or Moore) neighbourhood of the parental cell, as is illustrated in Figure S1. If a parent is scheduled to place a daughter agent on the lattice according to the von Neumann/Moore convention, then a daughter agent will be placed on a random lattice point in the 1st order von Neumann/Moore neighbourhood. However, if all lattice point in the 1st order neighbourhood (O.N.) are occupied by other agents, the daughter agent is instead placed on a random lattice point in the 2nd O.N. Further, if the 2nd O.N. is also completely occupied by agents, then the daughter agent is placed on a random lattice point in the 3rd O.N., and so on up to the νth O.N. It is up do the modeller to decide the value of ν, and in this study ν equals infinity in the *in vitro* monolayer case (with the restriction that agents can not be placed outside the lattice in the *in silico* implementation) and $\tilde{\nu} = 3$ in the spheroid case.

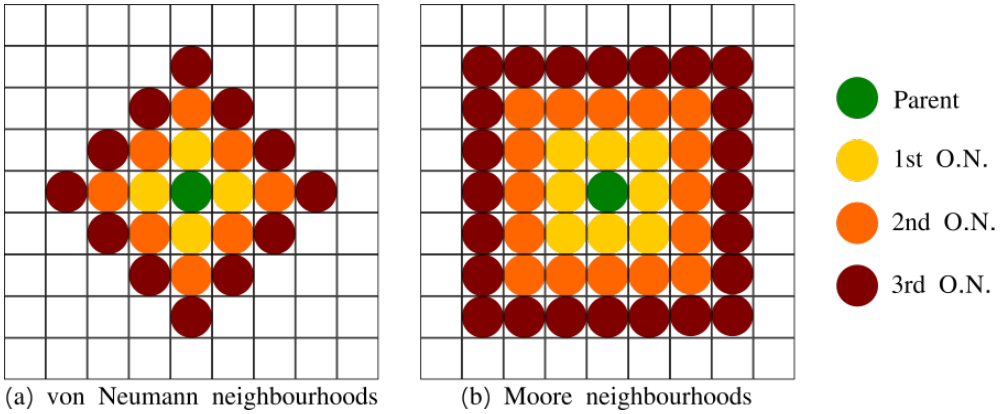

Figure S1: The 1st, 2nd and 3rd order neighbourhood (O.N.) of a parental agent using (a) the von Neumann convention and (b) the Moore convention.

S4 Cross-section to tumour spheroid extrapolation

When implementing our mathematical spheroid model, only a central cross-section of the tumour is actually simulated *in silico* and post simulation time this cross-section area (that is approximately circular) is extrapolated to a tumour volume (that is approximately spherical). From the extrapolated tumour spheroid, the two outputs $\tilde{X}_1$ (percentage of γH2AX-positive cells) and $\tilde{X}_2$ (tumour volume) are gathered. This is done by using simulated areas to compute the total tumour volume,

$$\tilde{X}_2 = \text{Total Tumour Volume} = \frac{4\pi}{3}\left(\frac{\text{Total Simulated Area}}{\pi}\right)^{3/2}, \tag{1}$$

and the quiescent tumour volume,

$$\text{Quiescent Tumour Volume} = \frac{4\pi}{3}\left(\frac{\text{Quiescent Simulated Area}}{\pi}\right)^{3/2}. \tag{2}$$

From the above, the volume of cycling, or proliferating cells, is obtained by

$$\text{Cycling Tumour Volume} = \text{Total Tumour Volume} - \text{Quiescent Tumour Volume}. \tag{3}$$

Now the output $\tilde{X}_1$ can be computed where,

$$\tilde{X}_1 = \text{Percentage of } \gamma\text{H2AX-positive cells in sphere} = \frac{\text{Number of simulated } \gamma\text{H2AX-positive cells}}{\text{Number of simulated cycling cells}} \times \frac{\text{Cycling Tumour Volume}}{\text{Total Tumour Volume}}. \tag{4}$$

S5 A note on simplifying modelling assumptions

Note that an agent in the spheriod setting can, in general, be chosen to comprise either one cancer cell or a group of cancer cells. Note also that modelling the spheroid tumour as a (spatially) two-dimensional disk means that the distribution of nutrients and drugs is modelled across a two-dimensional (rather than a three-dimensional) space. Likewise, the parameter $\tilde{\nu}$, that governs the allowed distance between a parental agent and its daughter agents, only concerns proliferation on a two-dimensional plane. By increasing $\tilde{\nu}$, the tumour will grow quicker and comprise a higher fraction of cycling (to quiescent) agents. Thus both the parameters $\tilde{\nu}$ and μ influence the rate of tumour growth in the spheroid simulation, and should ideally be fitted to match detailed spheroid data. In the current study, we choose to keep μ at the *in vitro*-calibrated value and thereafter fit $\tilde{\nu}$ to match the *in vivo* data. A modeller can chose to use a three dimensional spatial domain, and thus explicitly model a tumour spheroid instead of a tumour cross-section. Computational costs, fineness of available data, and the desired level of simulation details should be used to guide the choice of agents and spatial domain.

S6 A note on the choice of drug model

We assume all model parameters to be constant in time, including parameters pertaining to the doubling time of the cells. In the monolayer simulation, with some stochastic variability, this complies with Skipper's theoretical law on tumour growth rates which states that, in a tumour growing at a constant exponential rate, the doubling time of the tumour volume is constant over

the tumour's lifespan. Further, Skipper's law on tumour regression rates states that the fraction of cells killed by a given drug dose constant is constant (West and Newton, 2017). Although our drug-response model is stochastic, agent-based and concerns a DDR-inhibitor that targets cells in the DNA-damaged state D-S (rather than a general chemotherapy drug that targets cancer cells in other cell cycle states), the probability that a susceptible (D-S) cell is killed by a given drug dose is indeed constant, therefore the percentage of D-S cells killed by a given drug dose is constant (with some stochastic errors/in the large cell population limit). Furthermore, the fraction of cells entering the D-S state is constant and thus our current drug-response model upholds an "essence" of Skipper's tumour regression law. If one instead uses Gompertzian tumour growth models, in which the tumour growth rate varies over the tumour's lifespan, then drug-induced tumour regression can be modelled using the Norton-Simon hypothesis which states that tumor regression is linearly, positively correlated with the tumour growth rate at the time when the treatment is first applied.

S7 Residual plots

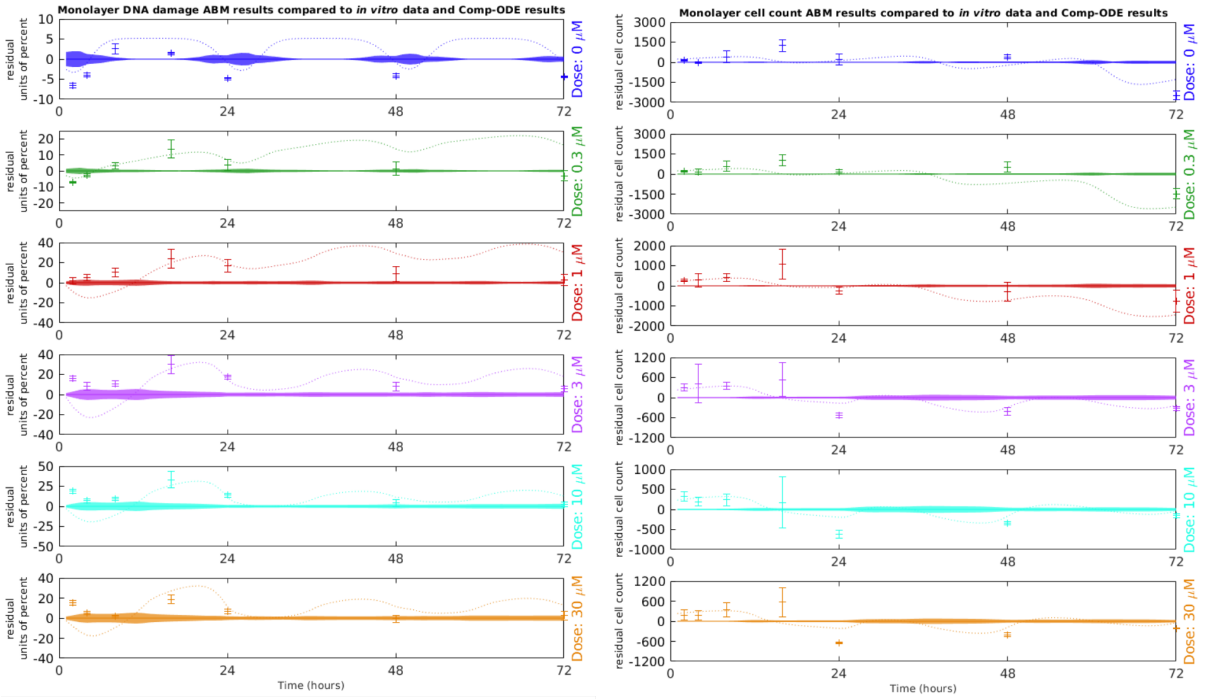

Figure S2: Residual plots for monolayer DNA damage (Left) and cell count (Right) simulation results for different drug doses. Simulation standard deviations are visualised with shaded ribbons. ABM simulation results are compared to *in vitro* data (with standard deviation error bars) (Checkley et al., 2015) and Checkley *et al.*'s compartment-ODE (Comp-ODE) model (Checkley et al., 2015) (dotted lines).

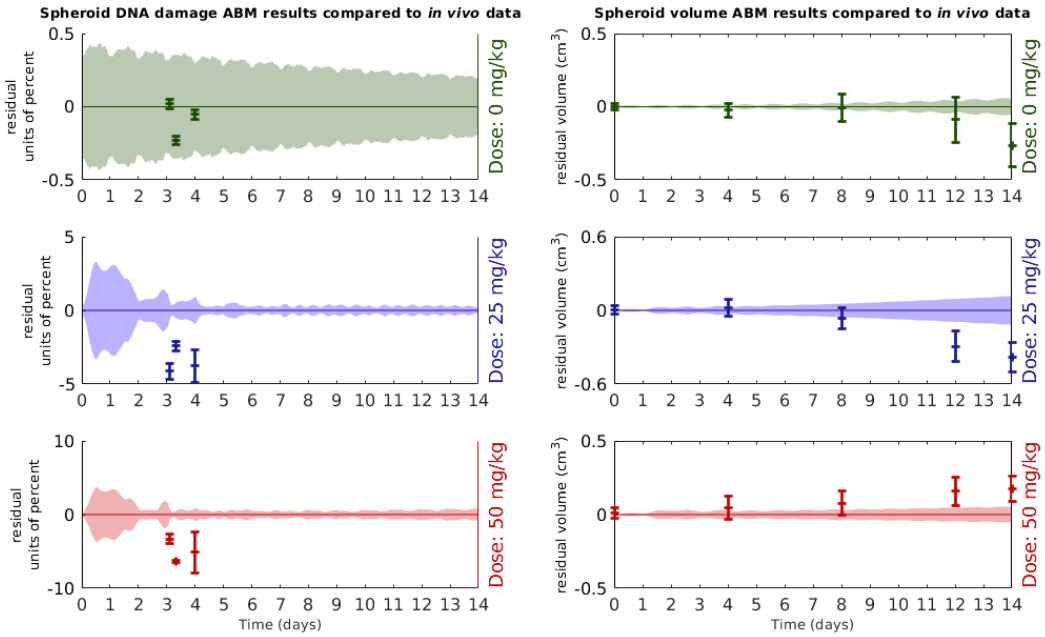

Figure S3: Residual plots where ABM spheroid simulations are compared to *in vivo* xenograft data (Checkley et al., 2015) at different drug doses. Simulation mean values and standard deviations are shown with solid lines and ribbons respectively. Data center points and error bars respectively show *in vivo* mean values and standard errors.

S8 Spheroid waterfall plot

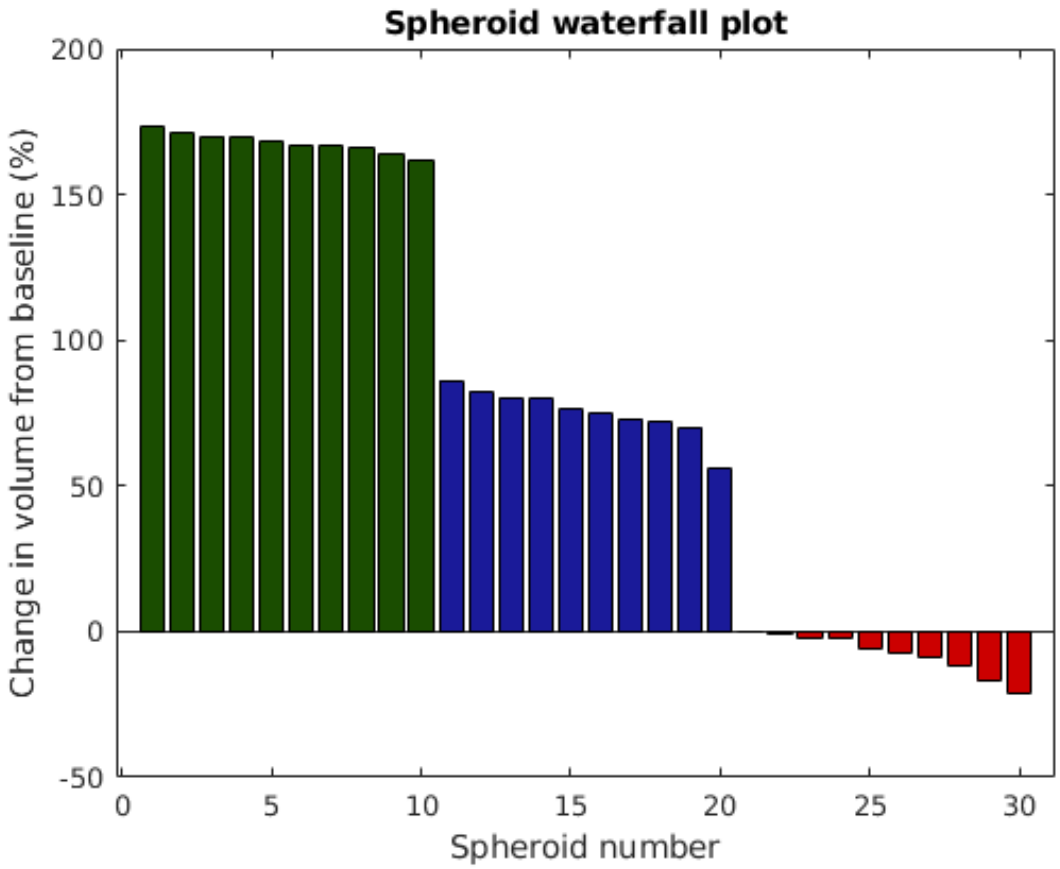

Figure S4: Waterfall plots showing the change in tumour volume at day 7 from the baseline (the tumour volume when treatment commences). Spheroids are subjected to drugs once daily at doses 25 mg/kg (blue bars) or 50 mg/kg (red bars). Green bars correspond to control cases (no drug).

S9 Uncertainty and Sensitivity Analyses

To evaluate the monolayer *in silico* findings obtained in our *in vitro* study, three uncertainty and sensitivity analyses techniques are performed. The three techniques are namely: (1) Consistency Analysis, which is used to determine how many *in silico* runs should be performed before defining results in terms of statistical metrics in order to mitigate uncertainty originating from intrinsic model stochasticity, (2) Robustness Analysis, which investigates model sensitivity to local parameter perturbations and (3) Latin Hypercube Analysis, which investigates model sensitivity to global parameter perturbations. These techniques are thoroughly described in a review/methodology paper (Hamis et al., 2020) which provides background information concerning the origin of these techniques as well as detailed information on how to implement them. To perform uncertainty and sensitivity analyses we need to specify a set of inputs and outputs. Here, the output variables are X_1: the percentage of γH2AX-positive (i.e. damaged) cells at the end time of the experiment (72 hours), and X_2: the cell count (i.e. the number of non-dead cells) at the end of the experiment. The input variables are the seven model parameters listed in Table 1, in the main article, that we calibrate using *in vitro* data. These inputs are namely μ, σ, Π_{D-S}, Θ_{D-S}, EC_{50}, γ and $T_{L\to D}$.

S9.1 Consistency Analysis

Results from the Consistency Analysis are provided in Figures S5, S6, S7, S8, S9 which show the $\hat{A}$-measures, in both computed and scaled forms, for the distribution sizes $n = 1, 5, 50, 100, 300$ respectively. By observing Figures S5 through to S9, it is clear that the statistical significance decreases with increasing distribution size n, as is shown in Figure S10 and Table S9.1 which show the maximal scaled $\hat{A}$-values for all tested distribution sizes. These results demonstrate that the distribution size $n = 100$ is the smallest tested distribution size that yields a small statistical significance (i.e. a maximum scaled $\hat{A}$-value smaller than 0.56) for both regarded output variables X_1 and X_2. From this we decide to base every *in silico* result (here in terms of mean values and standard deviations) on 100 simulation runs.

distribution size / output	n=1	n=5	n=50	n=100	n=300
X_1	1	0.92	0.61	0.55	0.54
X_2	1	0.84	0.59	0.55	0.54

Table S4: Maximal scaled $\hat{A}$-values produced in the Consistency Analysis for various distribution sixes n. The output variables are X_1, corresponding to the percentage of γH2AX positive (i.e. damaged) cells, and X_2, corresponding to the cell count.

S9.2 Robustness Analysis

We use Robustness Analysis to investigate how sensitive the output is to *local* parameter perturbations, that is to say when input parameters are varied one at a time. Figures S11, S12, S13, S14, S15, S16, S17 provide boxplots and $\hat{A}$-measures that demonstrate the effect that local perturbations of the input variables μ, σ, Π_{D-s}, Θ_{D-S}, EC_{50}, γ and $T_{L\to D}$ respectively have on the output variables X_1 and X_2. Key findings are listed below, discussing the impact of one input parameter at a time.

- Remarks regarding input parameter μ: Figure S11 shows that, for small parameter perturbations, increasing the average doubling times of cells, μ, overall decreases the percentage of γH2AX positive cells and increases the cell count, however this decrease/increase is not linear. This indicates that the results of the *in vitro* monolayer simulation (and of the *in vitro* experiment nonetheless) are sensitive to the *timing* of the drug administration. In other words, Robustness Analyses demonstrates that treatment responses depend on how many cells are in the susceptible cell-cycle state at time of drug administration.

- Remarks regarding input parameter σ: Figure S12 demonstrates that the level of cell cycle synchronisation amongst cells, quantified by the input σ, affects *in silico* outputs for small parameter perturbations. The results indicate that for highly asynchronised cells (i.e. high σ-values) the smoother growth curves yield higher cell counts at certain time-points (such as the end time 72 hours) and a lower percentage of γH2AX-positive cells. As discussed in the remark above, the timing between cell cycles and drug administration affect treatment responses.

- Remarks regarding input parameter Π_{D-S}: Figure S13 illustrates that increasing the probability that a cell enters the damaged S state, i.e. the variable Π_{D-S}, increases the percentage of γH2AX cells and decreases the cell count, as expected.

- Remarks regarding input parameter Θ_{D-S}: Figure S14 shows how the amount of time that damaged cells spend in the D-S state before attempting to repair, and thus the Θ_{D-S}-value, affects the output. Results show that the percentage of γH2AX positive cells increases with increasing values of Θ_{D-S}, as more damaged cells will accumulate in the D-S state. However, this does not affect the probability of cells repairing, so the cell count is not as sensitive to small perturbations of Θ_{D-S}. The value of $\Theta D-S$ implicitly affects the measured cell count at the end time of the experiment as a decreased/increased $\Theta D-S$-value yields a slightly decreased/increased time lag between a cell entering the D-S state and dying.

- Remarks regarding input parameter EC_{50}: Figure S15 demonstrates that output variables are highly sensitive to perturbations of EC_{50}. Increasing EC_{50} results in a higher percentage of γH2AX positive cells and a lower cell count. Thus the input parameter EC_{50} should be regarded as a highly influential on quantitative results.

- Remarks regarding input parameter γ: Figure S16 illustrates that output variables measured at the end time of the experiment are not very sensitive to small perturbations of γ.

This can be understood as the γ parameter inherently corresponds to 'how quickly' a drug achieves asymptotic behaviour in the E_{max} model, the model used in our mathematical framework to express cellular drug response.

- Remarks regarding input parameter $T_{L\rightarrow}$: Figure S17 shows how output variables change as a result of perturbations to the input variable $T_{L\rightarrow}$, that describes how long it takes for a cell that has failed to repair to die (i.e. how long a cell with a 'death-sentence' is picked up as γH2AX positive in the *in vitro* experiment). Results show that both the percentage of γH2AX positive cells and the cell count increases with increasing values of $T_{L\rightarrow}$, as dying cells will categorised as γH2AX positive longer before being categorised as dead. When calibrating the model, we avoid the effect of this input parameter by only regarding *in vitro* data at time points that are early enough to correspond to systems with no (or a negligible amount of) dead cells.

S9.3 Latin Hypercube Analysis

Latin Hypercube Analysis is here used to investigate how sensitive output responses are to *global* parameter perturbations. We here investigate parameter values within ranges that we consider to be 'plausible' from the calibration process and the Robustness Analysis. Figures S18, S19, S20, S21, S22, S23, S24 provide scatter-plots that demonstrate correlations between the output variables X_1 and X_2 and the input variables μ, σ, Π_{D-s}, Θ_{D-S}, EC_{50}, γ and $T_{L\rightarrow D}$ respectively. The Pearson Product Moment Correlation Coefficients between the various input-output pairs are listed in Table S9.3. To determine threshold values for correlation coefficient descriptors, we compromise between suggested values by other authors (Hamis et al., 2020), and take into account the fact that we are only regarding parameter values within 'plausible' ranges. With this as a guide, we here decide that our obtained correlation coefficients with a magnitude in [0,0.12] corresponds to the linear input-output relationship being 'negligible', [0.19, 0.35] 'weak', [0.48,0.59] 'moderate' and 0.84 'strong'. Key findings from the Latin Hypercube Analysis are listed below, where the impact of one input parameter is discussed one at a time.

- Remarks regarding input parameter μ: Figure S18 and the first column in Table S9.3 show that, for the allowed parameter range, μ and X_1 are moderately, negatively correlated as the correlation coefficient is -0.48 and the scatterplot displays an overall trend of the output (X_1) decreasing with increasing values of the input μ. The relationship between μ and the other output variable X_2 is, on the other hand, negligible. We explain this by the fact that treatment responses are sensitive to the timing of the drug administration, but there is a time-lag $T_{L\rightarrow D}$ between a cell's lethal event (failure to repair) and its death. As damaged (but not dead) cells are included in the cell count, the (μ,X_2)-relationship is more weakly linearly correlated than the (μ,X_1)-relationship.

- Remarks regarding input parameter σ: Figure S19 and the second column in Table S9.3 demonstrate that the linear relationships between input variable σ and the output variables X_1 and X_2 are both negligible, within the regarded input parameter value range.

- Remarks regarding input parameter Π_{D-S}: Figure S20 and the third column in Table S9.3 indicate that the relationships between the input variable Π_{D-S} and the output variables

X_1 and X_2 are, respectively, positively and negatively weakly linearly correlated. This agrees with the intuitive notion that if the probability that a cell enters the D-S state increases, cell damage (X_1) increases whilst the cell count (X_2) decreases.

- Remarks regarding input parameter Θ_{D-S}: Figure S21 and the fourth column in Table S9.3 show that the input variable Θ_{D-S} is has a negligible linear correlation with the output variables X_1 and X_2.

- Remarks regarding input parameter EC_{50}: Figure S22 and the fifth column in Table S9.3 demonstrate that the input variable EC_{50} impacts the output responses more than do other input variables, within the regarded ranges for input variables. EC_{50} is negatively, moderately linearly correlated with X_1 and EC_{50} is strongly, positively linearly correlated with X_2. These relationships are visually apparent in the regarded scatterplots.

- Remarks regarding input parameter γ: Figure S23 and the sixth column in Table S9.3 indicate negligible linear correlations between the input parameter γ and both output variables X_1 and X_2.

- Remarks regarding input parameter $T_{L\to D}$: Figure S24 and the last column in Table S9.3 demonstrate that the input variable $T_{L\to D}$ is positively, weakly, linearly correlated with the output X_1, whilst the linear correlation between $T_{L\to D}$ and X_2 is negligible.

input / output	μ	σ	Π_{D-S}	Θ_{D-S}	EC_{50}	γ	$T_{L\to D}$
X_1	-0.48	0.06	0.19	0.06	-0.59	0.05	0.35
X_2	0.12	0.01	-0.24	-0.02	0.84	0.12	0.00

Table S5: Pearson Product Moment Correlation Coefficients between input and output variables obtained in the Latin Hypercube Analysis.

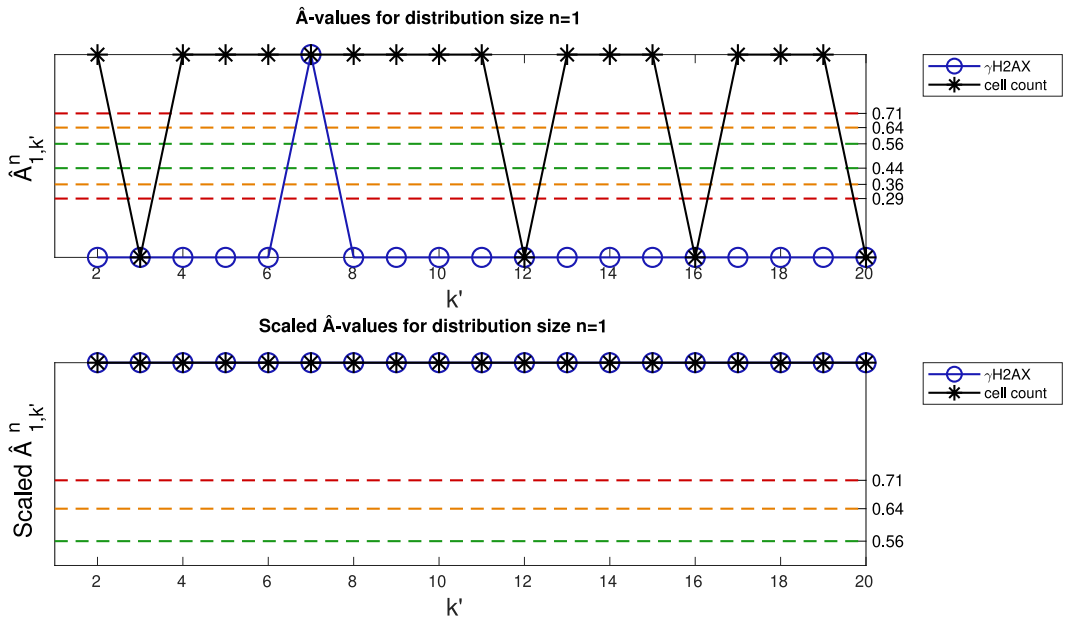

Figure S5: Consistency Analysis. $\hat{A}$-values in initial (top) and scaled (bottom) form for distribution size $n = 1$.

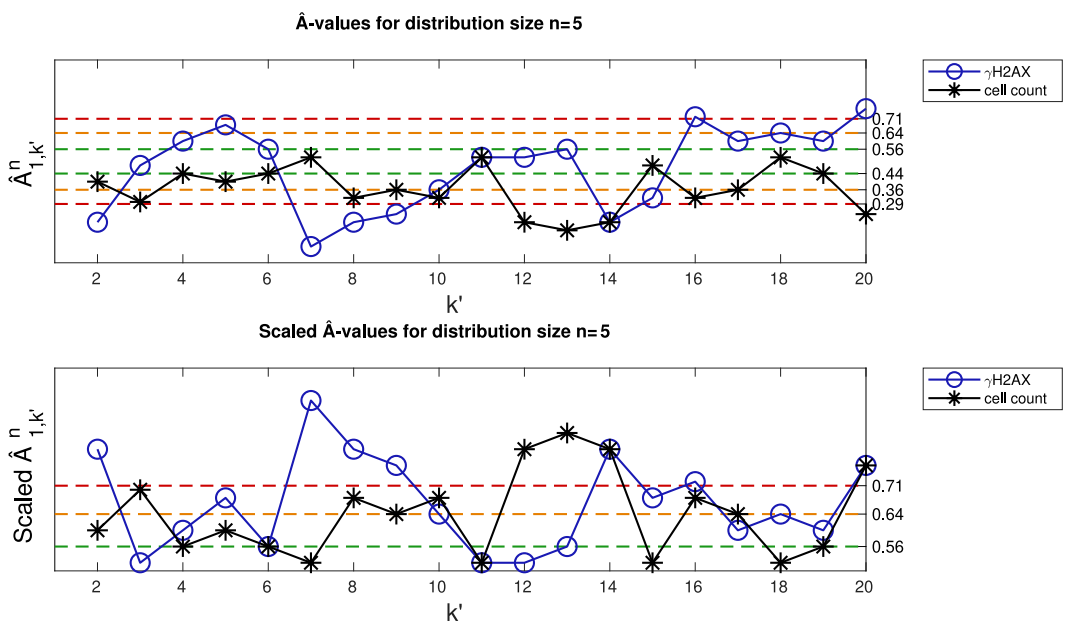

Figure S6: Consistency Analysis. $\hat{A}$-values in initial (top) and scaled (bottom) form for distribution size $n = 5$.

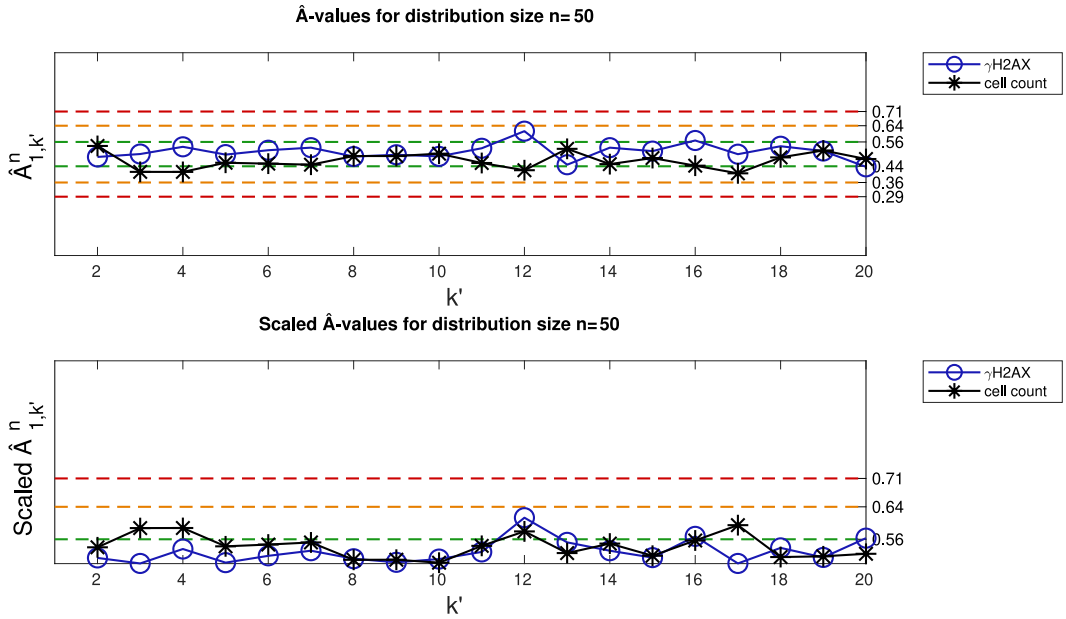

Figure S7: Consistency Analysis. $\hat{A}$-values in initial (top) and scaled (bottom) form for distribution size $n = 50$.

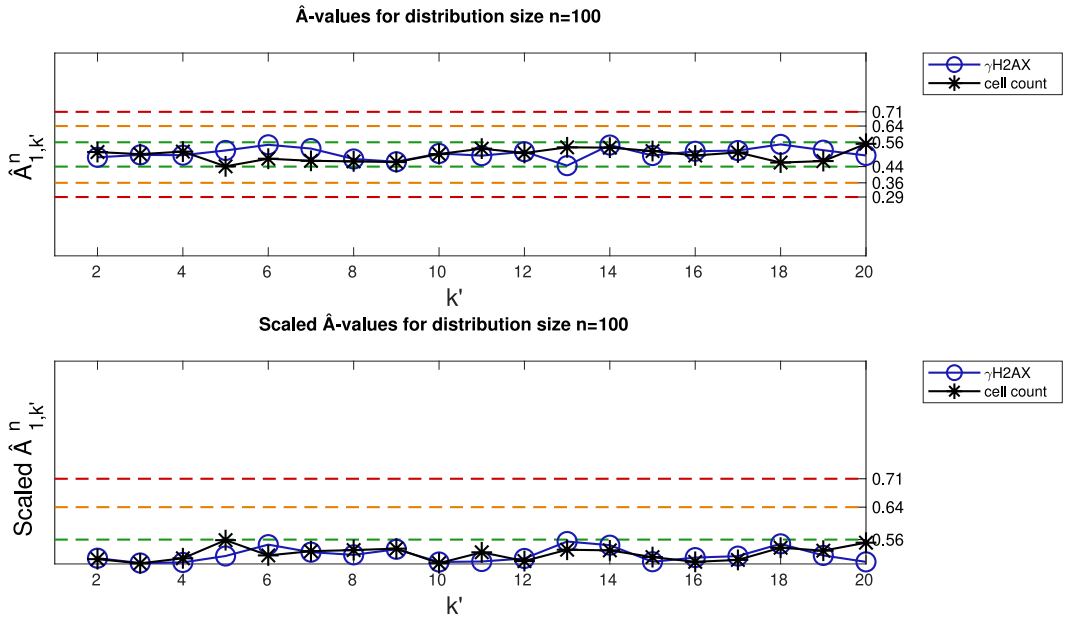

Figure S8: Consistency Analysis. $\hat{A}$-values in initial (top) and scaled (bottom) form for distribution size $n = 100$.

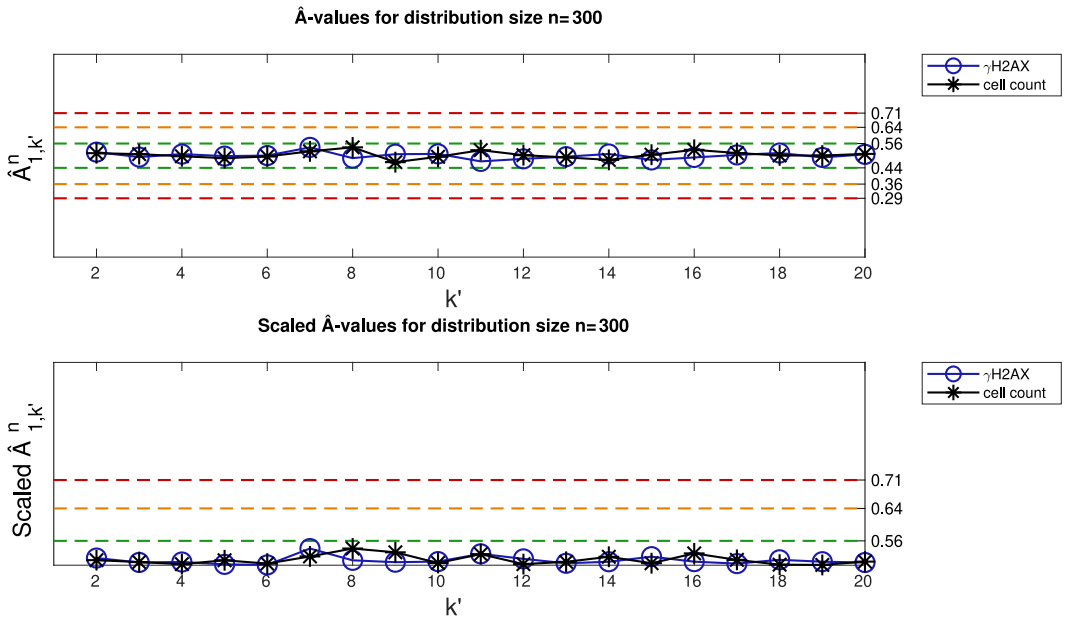

Figure S9: Consistency Analysis. $\hat{A}$-values in initial (top) and scaled (bottom) form for distribution size $n = 300$.

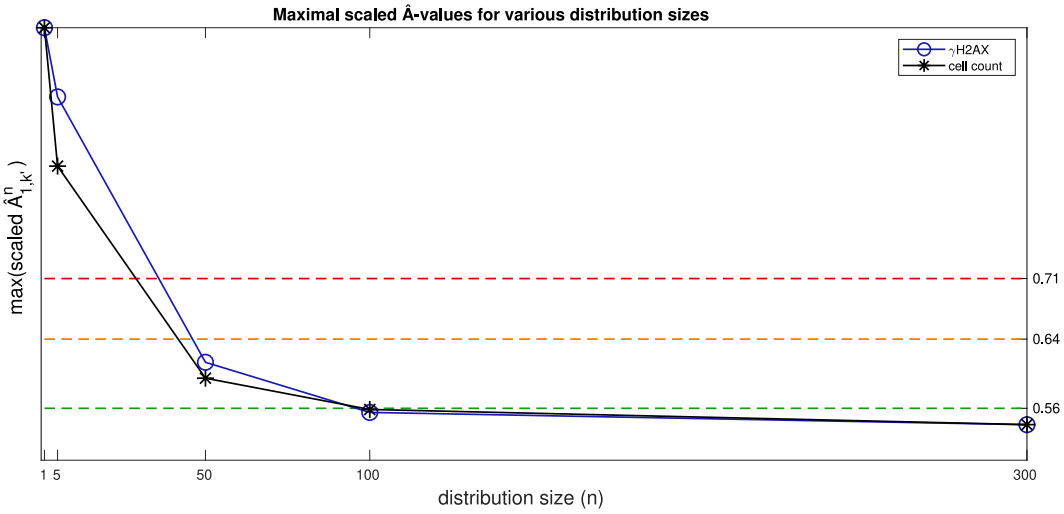

Figure S10: Consistency Analysis. Scaled $\hat{A}$-values for various distribution sizes tested in the Consistency Analysis.

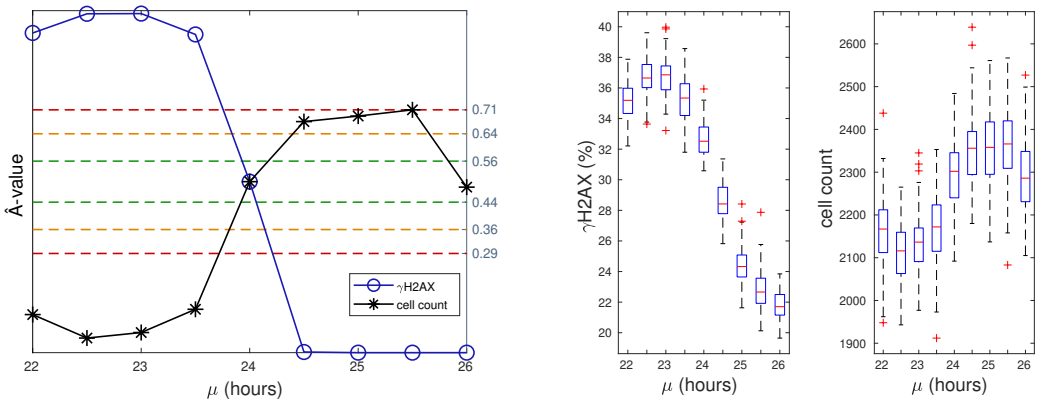

Figure S11: Robustness Analysis. Left: Output responses, in terms of percentage of γH2AX positive (i.e. damaged) cells, and cell count as a result of perturbations to the input variable μ. Right: Maximal $\hat{A}$-values resulting from comparisons between distributions with perturbed data and a distribution with calibrated (unperturbed) data.

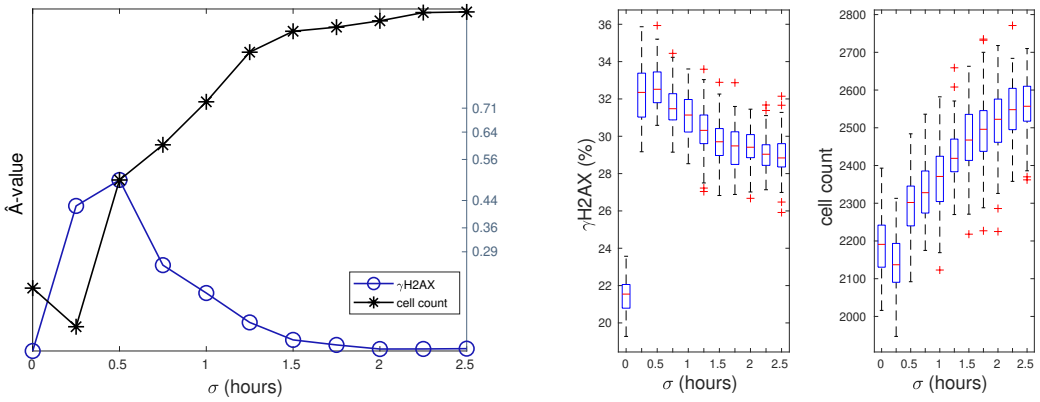

Figure S12: Robustness Analysis. Left: Output responses, in terms of percentage of γH2AX positive (i.e. damaged) cells, and cell count as a result of perturbations to the input variable σ. Right: Maximal $\hat{A}$-values resulting from comparisons between distributions with perturbed data and a distribution with calibrated (unperturbed) data.

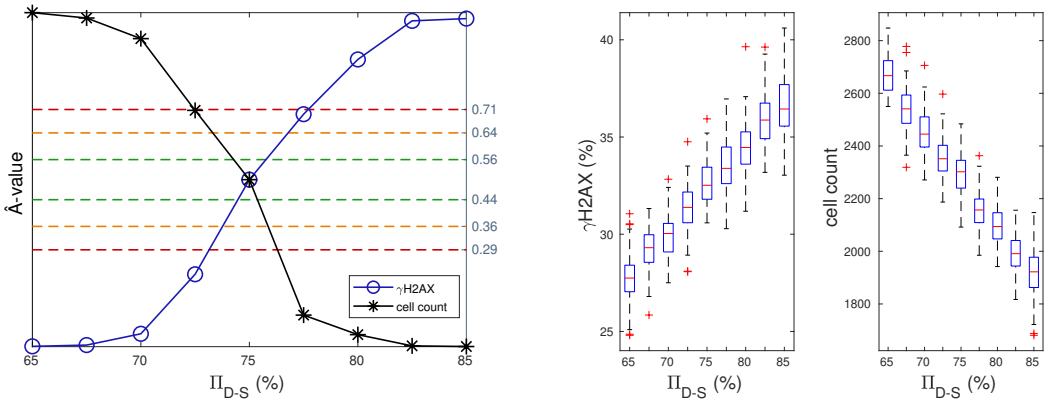

Figure S13: Robustness Analysis. Left: Output responses, in terms of percentage of γH2AX positive (i.e. damaged) cells, and cell count as a result of perturbations to the input variable Π_{D-s}. Right: Maximal $\hat{A}$-values resulting from comparisons between distributions with perturbed data and a distribution with calibrated (unperturbed) data.

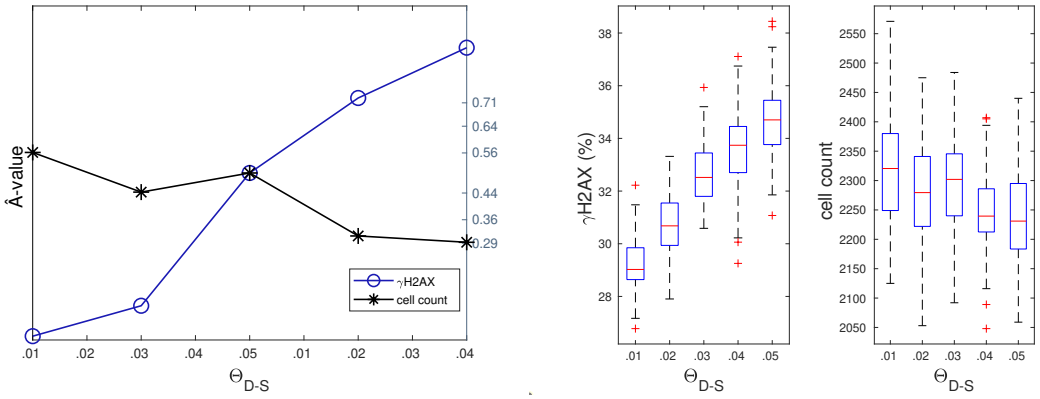

Figure S14: Robustness Analysis. Left: Output responses, in terms of percentage of γH2AX positive (i.e. damaged) cells, and cell count as a result of perturbations to the input variable Θ_{D-S}. Right: Maximal $\hat{A}$-values resulting from comparisons between distributions with perturbed data and a distribution with calibrated (unperturbed) data.

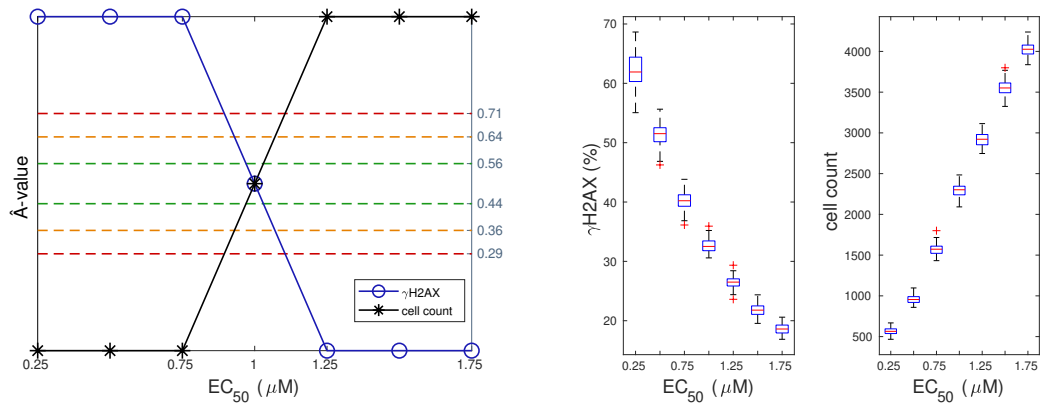

Figure S15: Robustness Analysis. Left: Output responses, in terms of percentage of γH2AX positive (i.e. damaged) cells, and cell count as a result of perturbations to the input variable EC_{50}. Right: Maximal $\hat{A}$-values resulting from comparisons between distributions with perturbed data and a distribution with calibrated (unperturbed) data.

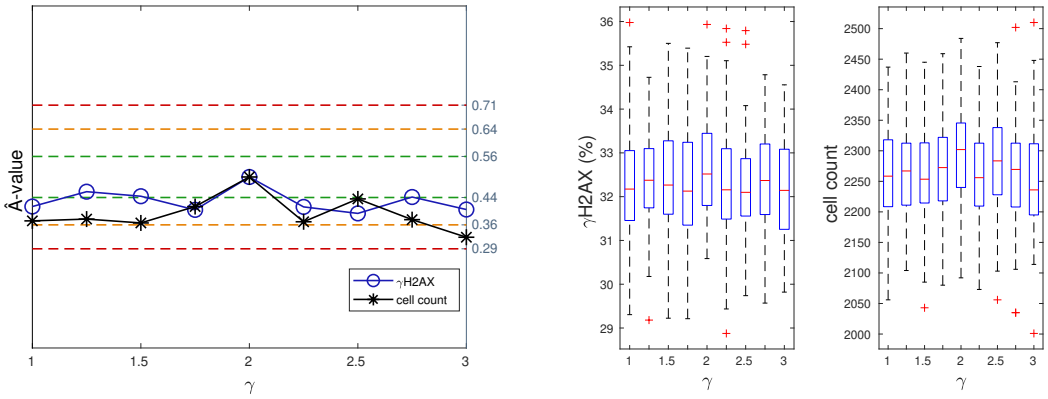

Figure S16: Robustness Analysis. Left: Output responses, in terms of percentage of γH2AX positive (i.e. damaged) cells, and cell count as a result of perturbations to the input variable γ. Right: Maximal $\hat{A}$-values resulting from comparisons between distributions with perturbed data and a distribution with calibrated (unperturbed) data.

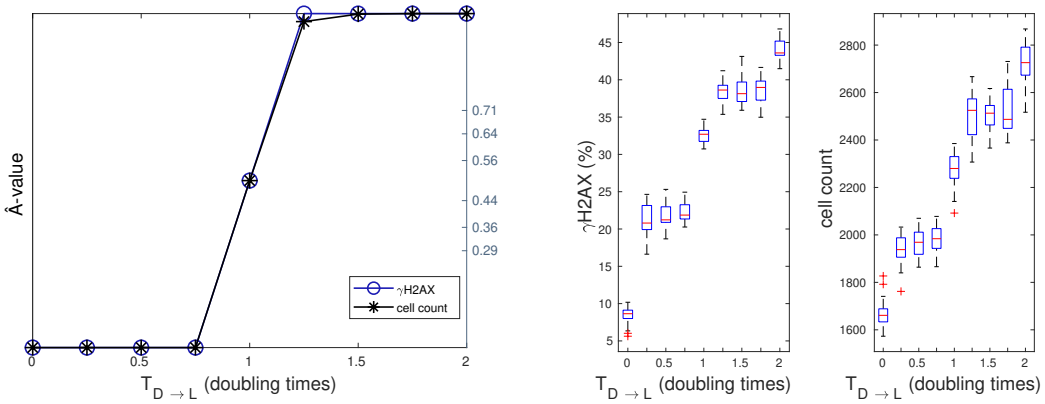

Figure S17: Robustness Analysis. Left: Output responses, in terms of percentage of γH2AX positive (i.e. damaged) cells, and cell count as a result of perturbations to the input variable $T_{D\to L}$. Right: Maximal $\hat{A}$-values resulting from comparisons between distributions with perturbed data and a distribution with calibrated (unperturbed) data.

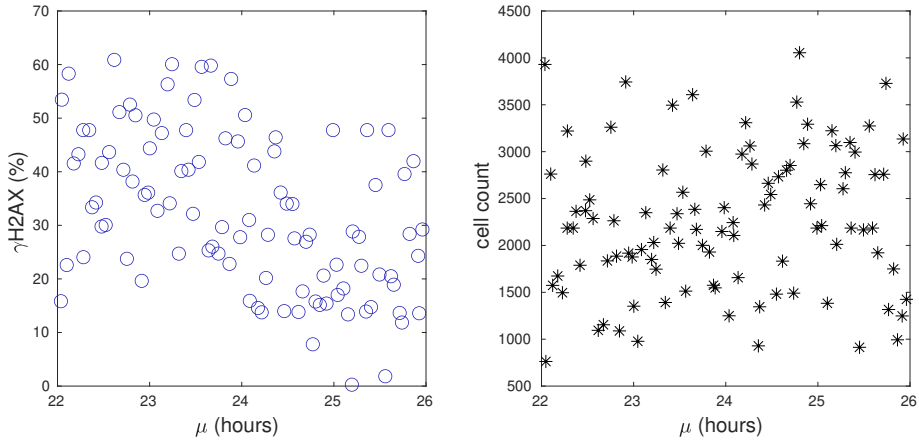

Figure S18: Latin Hypercube Analysis. Outputs in terms of γH2AX positive cells (left) and number of viable cells (right) when global parameter perturbations are performed. The scatterplots show the correlation between outputs and the input variable μ.

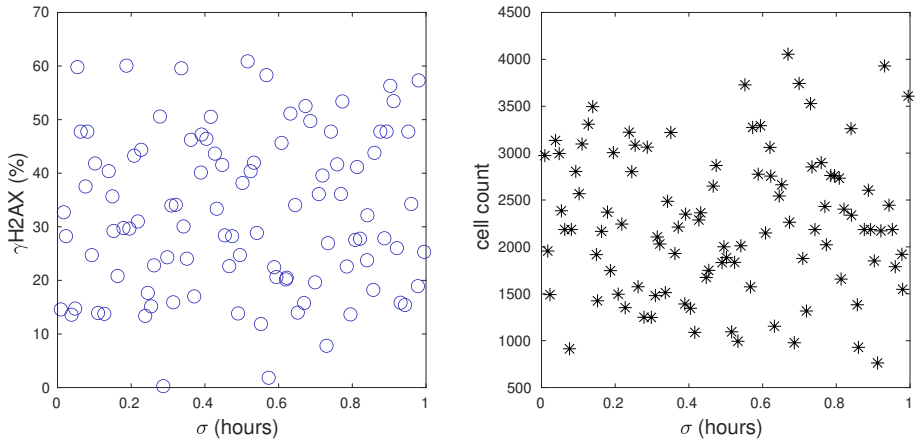

Figure S19: Latin Hypercube Analysis. Outputs in terms of γH2AX positive cells (left) and number of viable cells (right) when global parameter perturbations are performed. The scatterplots show the correlation between outputs and the input variable σ.

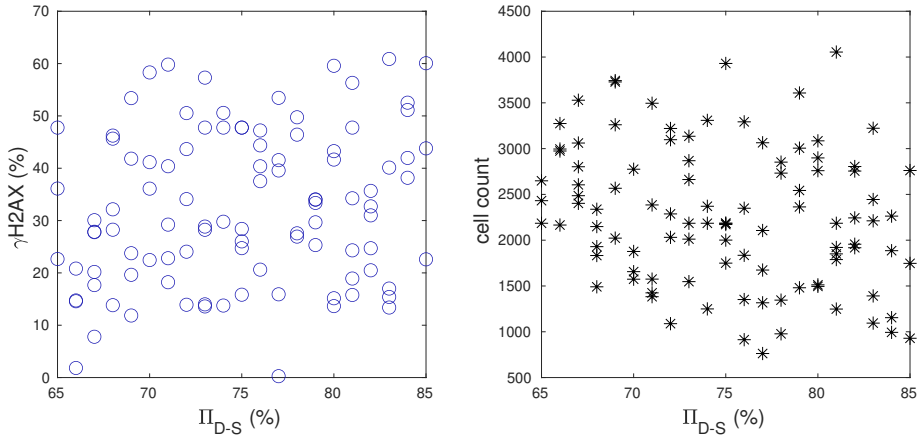

Figure S20: Latin Hypercube Analysis. Outputs in terms of γH2AX positive cells (left) and number of viable cells (right) when global parameter perturbations are performed. The scatterplots show the correlation between outputs and the input variable Π_{D-S}.

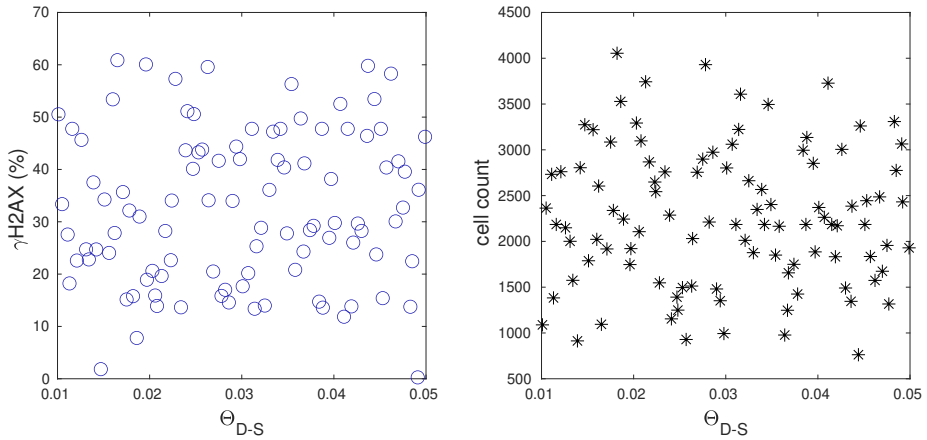

Figure S21: Latin Hypercube Analysis. Outputs in terms of γH2AX positive cells (left) and number of viable cells (right) when global parameter perturbations are performed. The scatterplots show the correlation between outputs and the input variable Θ_{D-S}.

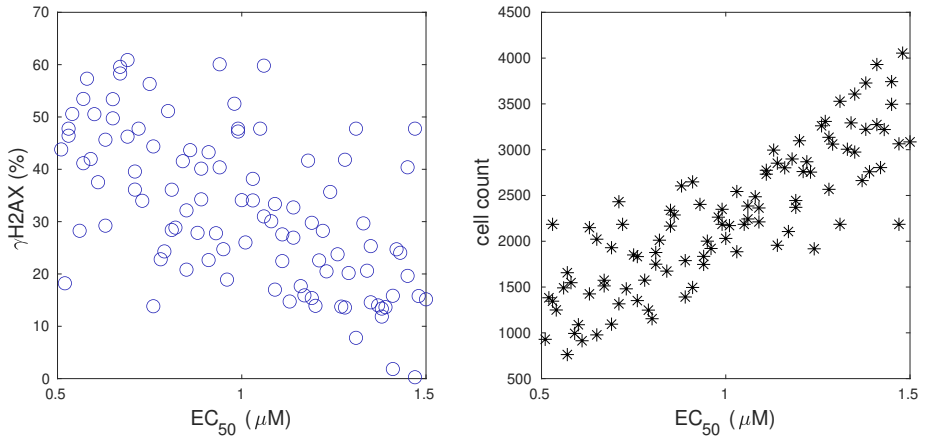

Figure S22: Latin Hypercube Analysis. Outputs in terms of γH2AX positive cells (left) and number of viable cells (right) when global parameter perturbations are performed. The scatterplots show the correlation between outputs and the input variable EC_{50}.

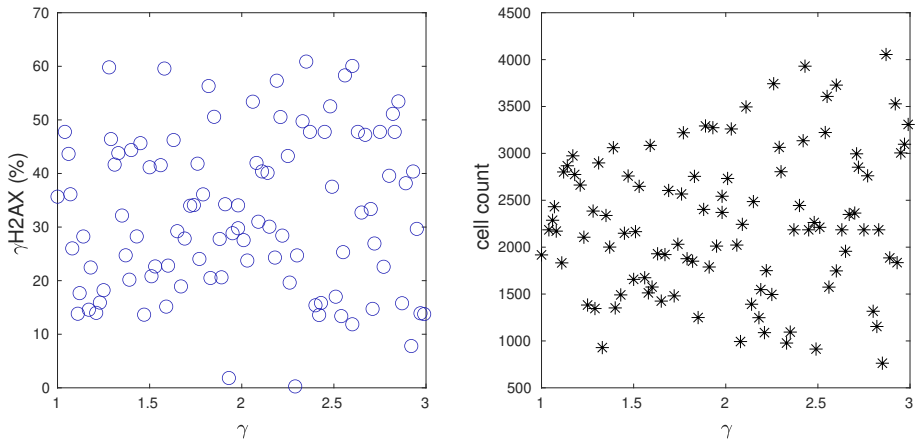

Figure S23: Latin Hypercube Analysis. Outputs in terms of γH2AX positive cells (left) and number of viable cells (right) when global parameter perturbations are performed. The scatterplots show the correlation between outputs and the input variable γ.

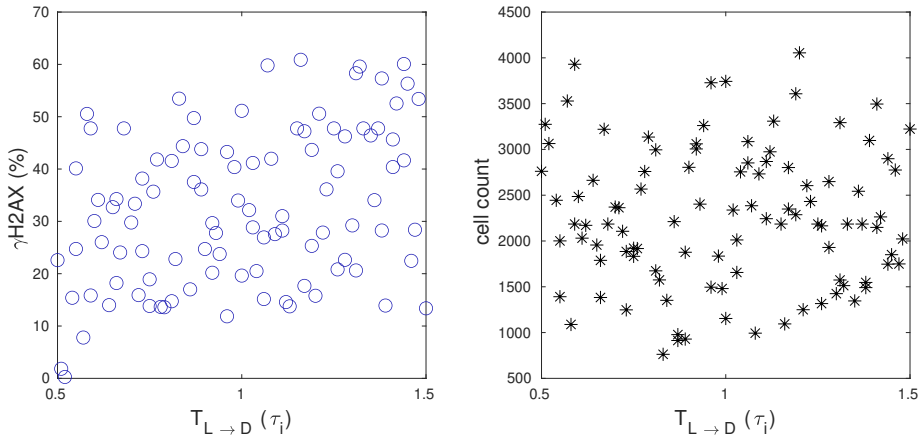

Figure S24: Latin Hypercube Analysis. Outputs in terms of γH2AX positive cells (left) and number of viable cells (right) when global parameter perturbations are performed. The scatterplots show the correlation between outputs and the input variable $T_{L\to D}$.

References

Checkley, S., MacCallum, L., Yates, J., Jasper, P., Luo, H., Tolsma, J., Bendtsen, C., 2015. Bridging the gap between in vitro and in vivo: Dose and schedule predictions for the ATR inhibitor AZD6738. *Sci Rep* **5**, 13545.

Hamis, S., Stratiev, S., Powathil, G.G., 2020. Uncertainty and sensitivity analyses methods for agent-based mathematical models: An introductory review. *The Physics of Cancer: Research Advances, ed. Bernard Gerstman, Singapore: World Scientific Publishing. Preprint: arXiv:1911.08429* .

Holford, N., 2017. Pharmacodynamic principles and the time course of immediate drug effects. *Transl Clin Pharmacol* **4**, 157–161.

West, J., Newton, P.K., 2017. Chemotherapeutic Dose Scheduling Based on Tumor Growth Rates Provides a Case for Low-Dose Metronomic High-Entropy Therapies. *Cancer Res.* **77**(23), 6717–6728.